IOPscience iopscience.iop.org

Home Search Collections Journals About Contact us My IOPscience

Ultrafast optical and far-infrared quasiparticle dynamics in correlated electron materials

This article has been downloaded from IOPscience. Please scroll down to see the full text article.

2002 J. Phys.: Condens. Matter 14 R1357

(http://iopscience.iop.org/0953-8984/14/50/203)

View the table of contents for this issue, or go to the journal homepage for more

Download details:
IP Address: 171.66.16.97
The article was downloaded on 18/05/2010 at 19:21

Please note that terms and conditions apply.

INSTITUTE OF PHYSICS PUBLISHING JOURNAL OF PHYSICS: CONDENSED MATTER

J. Phys.: Condens. Matter **14** (2002) R1357–R1390 PII: S0953-8984(02)33363-0

TOPICAL REVIEW

Ultrafast optical and far-infrared quasiparticle dynamics in correlated electron materials

R D Averitt[1] **and A J Taylor**

MST-10, Condensed Matter and Thermal Physics, Los Alamos National Laboratory, Los Alamos, NM 87544, USA

E-mail: raveritt@lanl.gov

Received 10 October 2002
Published 6 December 2002
Online at stacks.iop.org/JPhysCM/14/R1357

Abstract

We review the application of ultrafast optical spectroscopy in the study of correlated electron materials. The emphasis is on all-optical pump–probe and optical pump–far-infrared probe experiments on (a) colossal-magnetoresistance manganites and (b) high-temperature superconductors. The experimental techniques are discussed followed by a brief review of ultrafast electron dynamics in conventional wide-band metals which serves as a starting point in understanding the dynamics in more complex metallic systems. In the half-metallic manganites, the quasiparticle dynamics in the ferromagnetic metallic state can be understood in terms of a dynamic transfer of spectral weight which is influenced by the lattice and spin degrees of freedom. For the high-temperature superconductors, ultrafast quasiparticle dynamics are sensitive to the order parameter and superconducting pair recovery occurs on a picosecond timescale. These results show that, in general, ultrafast optical spectroscopy provides a sensitive method to probe the dynamics of quasiparticles at the Fermi level.

Contents

[1] Author to whom any correspondence should be addressed.

0953-8984/02/501357+34$30.00 © 2002 IOP Publishing Ltd Printed in the UK

List of abbreviations

UOS	ultrafast optical spectroscopy
CEMs	correlated electron materials
TMO	transition metal oxide
HMM	half-metallic manganite
HTSC	high-temperature superconductor
OPTP	optical pump–terahertz probe spectroscopy
THz-TDS	terahertz time-domain spectroscopy
FD	Fermi–Dirac
TTM	two-temperature model
CMR	colossal magnetoresistance
JT	Jahn–Teller
DSWT	dynamic spectral weight transfer
LAO	$LaAlO_3$
LCMO	$La_{0.7}Ca_{0.3}MnO_3$
LSMO	$La_{0.7}Sr_{0.3}MnO_3$
NSMO	$Nd_{0.7}Sr_{0.3}MnO_3$
BCS	Bardeen–Cooper–Schrieffer
YBCO	$YBa_2Cu_3O_7$
YPBCO	$Y_{0.7}Pr_{0.3}Ba_2Cu_3O_7$
BSCCO	$Bi_2Sr_2CaCu_2O_8$

1. Introduction

The allure of femtosecond optical spectroscopy in chemistry, biology and atomic and condensed matter physics is that, quite simply, it provides the ability to temporally resolve phenomena at the fundamental timescales of nuclear and electronic motion [1]. In condensed matter physics, the vast majority of research using ultrafast optical spectroscopy (UOS) has investigated the dynamics of electrons in semiconductors. This has contributed a great deal to our understanding of electron–electron (e–e) scattering, electron–phonon (e–p) scattering, electronic transport, coherence effects and the effects of quantum confinement upon these processes in semiconductor compounds and heterostructures [2]. More recently, ultrafast optical techniques have yielded insights into the many-body correlations that develop in photogenerated carrier distributions in semiconductors [3, 4]. Similarly, UOS has provided insight into the nature of e–e and e–p processes in conventional metals such as gold and silver [5–9]. There is an important difference in these studies as compared to semiconductors. In metals, the goal of UOS is to probe the dynamics of electrons at the Fermi level (E_F) to provide information about the low-energy electronic properties that complement, for example, specific heat or susceptibility measurements. There are of course difficulties, but there is

ample evidence that UOS does, in many instances, provide information regarding the low-energy excitations in metals.

It is worth mentioning that UOS of semiconductors and metals has benefited from advances in laser technology such as the development of extremely stable sub-100 fs lasers, and the development of chirped pulse amplification [10, 11]. The resultant increases in stability and sensitivity have allowed researchers to focus their efforts on the materials as opposed to keeping the laser system running for the duration of an experiment thereby helping to bring UOS to the level of a complementary research tool. These advances have also enabled researchers to push femtosecond optical methods from the visible through the mid-infrared to the far infrared using techniques such as optical parametric generation or amplification, difference frequency generation or resonant excitation of biased semiconductor striplines [12–14].

Concurrent with the advances in femtosecond lasers and their application to understand fundamental physical phenomena in semiconductors and metals were the tremendous advances in the preparation and physical understanding of correlated electron materials (CEMs). Certainly, the starting point for a great deal of this research was the discovery of high-temperature superconductivity in doped transition metal oxides (TMOs) [18]. The advances in crystal growth and thin-film technology that came about from this discovery have led to a flurry of activity in other doped TMOs, the most ubiquitous example being the manganites [19]. Underlying all of this work is the desire to understand the interplay between the spin, lattice, charge and orbital degrees of freedom in determining the ground-state properties of CEMs. As such, it is important that well established experimental techniques are utilized to unravel the contributions of these competing degrees of freedom. In addition, new experimental techniques must be brought to bear on the difficult problems posed by CEMs [20]. UOS falls under both of these headings—UOS has been around for some time, but until recently it was scarcely applied to CEMs. The goal of this topical review, then, is to demonstrate that UOS can be fruitfully applied to the study of CEMs, using as a foundation the many results that have been obtained on simpler (e.g. fewer-competing-degrees-of-freedom) materials such as conventional metals and semiconductors.

We hope to achieve this goal by way of example. The examples we will discuss in some detail are (a) the half-metallic manganites (HMMs) and (b) high-temperature superconductors (HTSCs). We will proceed as follows: first we will briefly introduce the techniques of all-optical pump–probe spectroscopy and, in more detail, optical pump–terahertz probe spectroscopy (OPTP). Then, the ultrafast electron dynamics in conventional metals will be considered since this can serve as a useful starting point in understanding ultrafast dynamics in CEMs. Next, we will present UOS experiments of quasiparticle dynamics in HMMs. It will be shown that UOS is sensitive to the spin degree of freedom and that below the Curie temperature it is possible to acquire some understanding of the relative importance of spin disorder versus thermally disordered phonons in determining the conductivity. Then the ultrafast dynamics of HTSCs will be presented. We will show that UOS of superconductors is sensitive to the opening of the gap (both the superconducting gap and the pseudogap) and processes that determine the pair recombination time following optical excitation. In particular, we will see that using OPTP, it is possible to probe the dynamics of quasiparticles and Cooper pairs simultaneously and that the far-infrared studies are in reasonable agreement with all-optical dynamics. Finally, we will conclude and suggest some directions for future research in applying UOS to the study of CEMs. Again, the goal of this brief review is to demonstrate the utility of UOS in studying CEMs. Therefore, there are sure to be important articles we neglect to cite—we apologize for this in advance.

2. Experimental techniques

Figure 1 shows the general idea of pump–probe experiments. A short optical pump pulse having centre frequency ω_1 induces a change in the sample. Subsequently, a pulse with centre frequency ω_2 probes the pump-induced changes in the sample. The temporal evolution is measured by delaying the relative arrival time of the pump and probe pulses using a precision mechanical delay line. In principle, the details of the experiment are related to what is measured—i.e. the change in the probe reflectivity, transmission or polarization. Pump–probe spectroscopy falls under the domain of nonlinear optics and can be formally described in terms of the third-order nonlinear optical susceptibility $\chi^{(3)}(\omega)$. Specifically, a nonlinear polarization is generated in the sample which serves as a source term in the electromagnetic wave equation that can then be used to describe changes in the probe pulse due to propagation in the photoexcited material. This approach is cumbersome at best in attempting to describe the dynamics of electrons in condensed matter systems. Another approach (though ultimately equivalent) is to try and describe the dynamics in terms of changes in the complex dielectric function $(\epsilon_1 + i\epsilon_2)$ of the sample since these are the constitutive relations that are more common (and therefore lend greater intuition) in describing the electronic properties of materials. For example, in many femtosecond experiments on metals, the dynamics are interpreted using the equation

$$\frac{\Delta\Upsilon}{\Upsilon}(t) = \frac{\partial \ln(\Upsilon)}{\partial \epsilon_1}\Delta\epsilon_1(t) + \frac{\partial \ln(\Upsilon)}{\partial \epsilon_2}\Delta\epsilon_2(t) \tag{1}$$

where Υ is the reflectivity R or transmission T, and $\Delta\epsilon_1$, $\Delta\epsilon_2$ are the induced changes in the real and imaginary parts of the dielectric function, respectively. Having some insight into the electronic properties described by $\epsilon_1 + i\epsilon_2$ (or as we shall see, the complex conductivity $\sigma_1 + i\sigma_2$) serves as a useful starting point to understand the dynamics described by $\Delta\epsilon_{1,2}(t)$. There is of course the very difficult problem of modelling the dynamics—useful approaches include simple rate equations, density matrices or the Boltzmann transport equation. All of these theoretical approaches have been used to provide insight into the electron dynamics and electronic properties of many materials.

2.1. Optical pump–probe spectroscopy

The most utilized ultrafast optical technique is optical pump–probe spectroscopy in which the photoinduced changes in the reflectivity or transmission of a sample are measured in the visible or near-IR region of the electromagnetic spectrum. While shorter pulses have been generated, the current state of the art for temporal resolution in UOS is ∼10–20 fs. The pump beam is focused to a diameter that is somewhat larger than the probe beam to ensure spatially homogeneous excitation. The pump:probe intensity ratio is typically greater than 20:1 to minimize self-induced nonlinearities of the probe beam. Lock-in detection is usually employed with the pump beam modulated using a mechanical chopper or an acousto-optic modulator. The latter technique provides a greater sensitivity since acousto-optic modulation can be performed at considerably higher frequencies than mechanical chopping (e.g. 2 kHz versus 100 kHz or higher), thus reducing $1/f$ noise. It is possible to detect changes in $\Delta R/R$ of $\sim 10^{-6}$ in optimized experiments (for experiments using regenerative amplifiers the sensitivity is considerably lower, $\sim 10^{-4}$). For degenerate pump–probe spectroscopy, polarization discrimination is typically employed to minimize pump scatter on the detector which can easily overwhelm the induced change of the probe beam. Other discrimination techniques include wavevector discrimination and, in the case of nondegenerate pump–probe spectroscopy, spectral discrimination. A powerful technique in UOS is to measure the

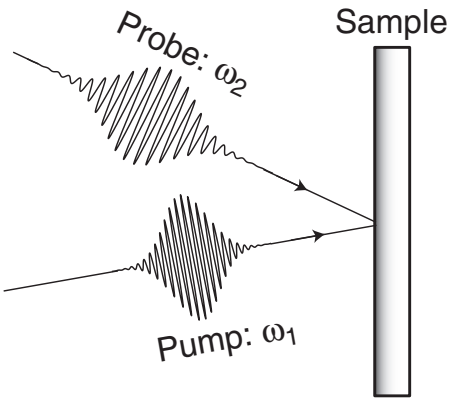

Figure 1. A pump pulse with centre frequency ω_1 excites the sample and a probe pulse with centre frequency ω_2 probes the induced change. All-optical experiments and optical pump–THz probe experiments are the same in principle with the difference being in how the radiation is generated and detected.

dynamics as a function of wavelength by either tuning the probe wavelength or by using a spectrometer. As we will see, this is an important difference in comparison to OPTP which utilizes Fourier transform methods to obtain spectrally resolved data.

2.2. Terahertz time-domain spectroscopy

One of the most important advances in femtosecond optics during the past 15 years has been the development of terahertz time-domain spectroscopy (THz-TDS) [12–14]. This is a powerful coherent free-space time-gated technique that is being broadly applied to problems in condensed matter physics [15], liquid and gas-phase molecular spectroscopy [16] and imaging science [17], to name a few examples. Excellent reviews of THz-TDS have been published [21–23]. Here we briefly mention the details before moving on to optical pump–THz probe spectroscopy. THz-TDS is a far-infrared spectroscopic method in which nearly single-cycle electromagnetic field transients are generated and detected using $\sim$100 fs optical pulses. The coherent nature of THz-TDS yields a much greater brightness in comparison to thermal sources and optical gating discriminates against the thermal background leading to, in some cases, a signal-to-noise ratio approaching 10^5. Perhaps most important of all is that THz-TDS measures the electric field (i.e. amplitude and phase) of the THz pulse with high linearity.

Two different approaches have been used to generate and detect THz pulses: resonant photoconductive switching and nonresonant optical rectification in electro-optic crystals [12–14]. Historically, THz-TDS using photoconductive switching was developed before electro-optically based THz-TDS. The output of a Ti:Al_2O_3 laser is split into a generating beam and a gating beam. For THz generation, femtosecond optical pulses are tightly focused onto a DC-biased coplanar stripline which has been deposited on a semiconductor (e.g. radiation-damaged silicon on sapphire, GaAs or low-temperature-grown GaAs). The optical pulse creates electron–hole pairs that are accelerated in the bias field. This ultrafast photoinduced current transient coherently radiates a nearly single-cycle THz pulse (e.g. $E_{\mathrm{THz}}(t) \sim \partial J(t)/\partial t$). At the detector, the THz pulse is temporally coincident with the optical gating pulse and provides a voltage bias to accelerate the optically generated carriers, resulting in a current that can be measured using current amplification and lock-in detection.

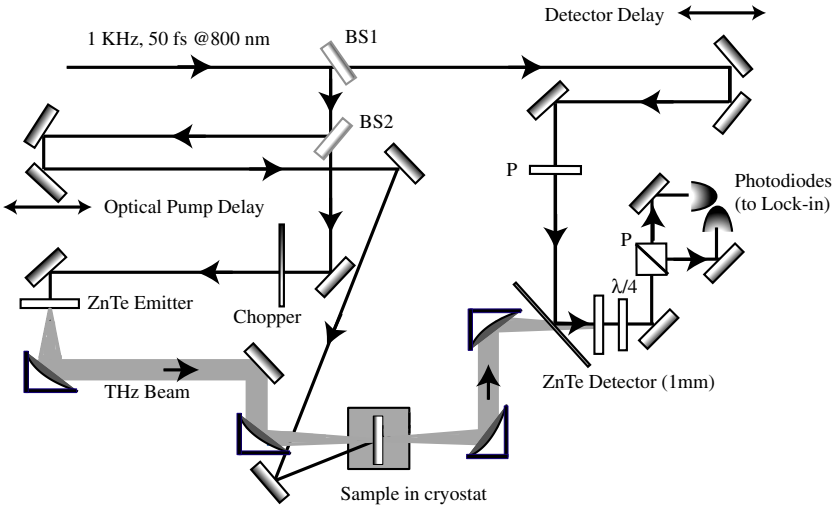

Figure 2. THz-TDS and OPTP set-up. BS1 reflects approximately 95% of the light with the remaining 5% used as the gate beam to detect the THz pulses. BS2 is a 50:50 beamsplitter and allows for the incorporation of a pump beam for OPTP experiments (reproduced with permission from [33]).

Nonresonant electro-optic generation and detection is quite similar to the photoconductive set-up and an example is shown in figure 2. In this case the emitter is an electro-optic crystal ($\langle 110 \rangle$ oriented ZnTe in the most common emitter and detector material). Difference-frequency generation in the ZnTe crystal occurs between the different wavelengths that comprise the optical pulse resulting in a spectrally broad THz pulse (in this case $E_{\mathrm{THz}}(t) \sim \partial^2 P(t)/\partial t^2$ where $P(t)$ is the induced polarization). The THz pulse is focused onto the sample using an off-axis paraboloidal mirror, recollimated and then focused on the detector which is also ZnTe. The THz pulse induces a birefringence in the ZnTe detector which results in a change in the polarization of the optical gate beam. Using a quarter waveplate and a polarizing beamsplitter, the THz electric field is measured as an amplitude modulation of the optical beam. Figure 3(a) shows a typical THz pulse generated and detected using a Ti:Al_2O_3 regenerative amplifier producing a 50 fs 1.5 eV pulse at 1 kHz with the set-up as in figures 2. Figure 3(b) shows the amplitude spectrum obtained from Fourier transformation of the pulse. The useful frequency content extends from approximately 100 GHz to 2.5 THz. Resonant and nonresonant methods have been used to generate much higher frequencies, but spectroscopic measurements using such sources is currently the exception rather than the rule [4, 24, 25].

For spectroscopy, a measurement is made using a suitable reference followed by measuring the desired sample. For example, for a thin metallic film on a insulating substrate, the reference is an uncoated substrate. Dividing the Fourier transform of the time domain sample data $E_{sam}(t)$ and reference data $E_{ref}(t)$ gives the complex transmissivity $T(\omega) = E_{sam}(\omega)/E_{ref}(\omega)$. Using the appropriate complex Fresnel equation, the complex dielectric function or complex conductivity can be numerically solved without any model assumptions. For the case of a metallic film on a insulating substrate the complex Fresnel equation can be simplified yielding the following expression for the complex transmissivity:

$$T(\omega) = \frac{E_{sam}(\omega)}{E_{ref}(\omega)} = \frac{1 + n_3}{1 + n_3 + Z_o \sigma(\omega) d} \exp(\mathrm{i}(\omega/c)\Delta L(n_3 - 1)). \tag{2}$$

Here n_3 is the complex index of refraction of the substrate, Z_o is the free space impedance,

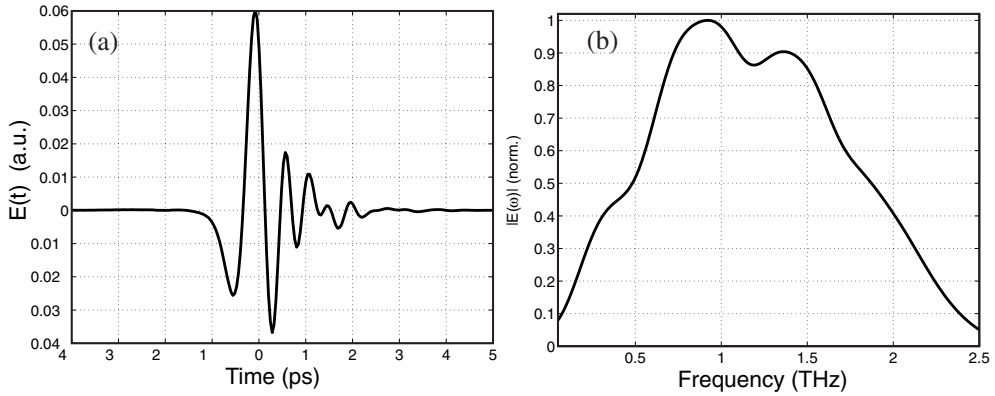

Figure 3. (a) Typical THz electric field profile in the time domain. (b) Amplitude spectrum versus frequency of the pulse in (a).

$\sigma(\omega) = \sigma_1(\omega) + i\sigma_2(\omega)$ is the complex conductivity, d is the metal film thickness and ΔL is the difference in thickness between the sample substrate and reference substrate. This expression includes the multiple reflections in the metal film but does not include the multiple reflections from the substrate since the reflections are temporally windowed in the experiment. The assumptions in deriving this expression from the full Fresnel equation are $\check{n} \gg n_3 > 1$ and $d\check{n}\omega/c \ll 1$ where $\check{n}$ is the complex index of the metal film. For the manganites and superconductors discussed below, it was verified that this expression is essentially exact by comparing it to the full numerical solution of the Fresnel equation at all temperatures (i.e. it is valid for the smallest conductivities we have measured).

2.3. Optical pump–terahertz probe spectroscopy

The extension of THz-TDS to OPTP is quite simple as shown in figure 2. All that is required is the addition of a beam splitter (BS2 in figure 2), an additional mechanical delay line, and steering mirrors to direct the optical pulses to the sample. The optical beam induces a change in the sample and the resulting change in the terahertz transmission is measured. For the CEM studies, this can be thought of as measuring changes in the complex conductivity of a sample with picosecond resolution. It should be noted that in comparison to all-optical pump–probe spectroscopy there are two delay lines (the optical pump line, and the THz gate line) which complicates matters as discussed below. It was realized early on that this technique has application in probing dynamics in condensed matter [26, 27]. However, in the past few years, with the developments of electro-optic techniques coupled with regenerative amplifiers, OPTP has dramatically advanced in its utility. Besides the CEM examples discussed here, OPTP has found application, for example, in probing the dynamics of photogenerated electrons in semiconductors and liquids [28–32].

The ability to directly measure induced changes in the far-IR conductivity is the main advantage of OPTP in comparison to all-optical methods. That is, in OPTP the THz pulse directly probes the low-lying electronic structure (averaged over the Fermi surface) whereas all-optical methods generally measure changes in the joint density of states between the occupied and unoccupied levels which can complicate interpreting the dynamics. Another advantage of OPTP is that it is possible to measure induced changes in the real and imaginary conductivity. This, as discussed below, enables simultaneous measurement of the dynamics of quasiparticles and the superconducting condensate. OPTP does have a lower sensitivity and the temporal

resolution is inherently lower than all-optical measurements since the THz probe pulse (see figure 3(a)) is approximately 1 ps in duration.

There are different ways to acquire data in an OPTP experiment and care must be used so as to not misinterpret the data. For both methods it is useful to move the chopper to the optical pump beam since this yields a zero-background measurement and the changes are directly measured at the chopper frequency, thereby increasing the sensitivity. The first method to obtain dynamics is to position the gate delay at the peak or null point of the THz electric field. Then the dynamics are measured by scanning the optical pump delay line to map out the dynamics. This one-dimensional method measures the dynamics averaged over the frequency content of the THz pulse. This is the quickest method to obtain conductivity dynamics though it must be kept in mind that the optical pump can induce changes in the amplitude and phase of the THz probe pulse. For example, if the pump induces measurable changes in σ_1 and σ_2, then there will be appreciable amplitude and phase changes in the transmitted THz electric field and simply scanning the optical pump delay results in data that contain both of these changes and are difficult to interpret. This is exactly the case for high-T_C materials since, below T_C, optical pumping induces considerable changes in σ_1 (related to the quasiparticle fraction) and σ_2 (dominated by the pair fraction) meaning that this simple one-dimensional scanning technique is not appropriate. On the other hand, in the HMMs, the THz conductivity in the ferromagnetic metallic state is dominated by a Drude-like response and optical excitation results in changes in σ_1 (there are changes in σ_2 of course, but the magnitude is so small that the pump-induced phase change of the THz electric field is minimal). Thus, for the manganites it is possible to use this one-dimensional technique to directly probe the conductivity dynamics.

The second data acquisition method for OPTP experiments is a two-dimensional technique where the delay of the optical pump line is set to a fixed time delay t_p (relative to the arrival of the THz pulse at the sample), and then the gate line is scanned. This yields, if the optical pump line is chopped, a waveform that corresponds to the induced change in the THz electric field ($\Delta E(t, t_p)$). By measuring this waveform at different values of t_p, it is possible to follow the evolution of the induced changes in the amplitude and phase of the THz electric field. For a specific t_p, the induced change in conductivity is obtained as described above for THz-TDS, except now $E_{sam}(t, t_p) = E_{sam} + \Delta E(t, t_p)$ is used in the Fourier transform to obtain the complex transmissivity $T(\omega, T_L)$ from which $\sigma(\omega, t_p)$ is obtained. We use this method in analysing the OPTP data on the high-T_C superconductors below. However, it is crucial to emphasize that this approach is only an approximation and is best used when the induced changes in conductivity are (a) small and (b) vary slowly in comparison to the duration of the THz pulse. In fact, this prescription is formally incorrect and can lead to errors in interpreting the conductivity dynamics. This has been explicitly discussed for the case of high-T_C materials [33], and in more general terms as well [34–36]. This can be understood as follows. In THz-TDS, we have seen that (equation (2)) $E_{sam} = T(\omega)E_{ref}$. In the time domain this is a convolution between $E_{ref}(t)$ and the response function $T(t)$ which is just the inverse Fourier transform of $T(\omega)$.

$$E_{sam}(t) = \int_{-\infty}^{t} E_{ref}(\tau)T(t-\tau)\,\mathrm{d}\tau. \tag{3}$$

However, in OPTP this description in terms of a linear response is no longer valid since another time variable (t_p) must be considered. That is, equation (3) in OPTP becomes

$$E_{sam}(t, t_p) = \int_{-\infty}^{t} E_{ref}(\tau)T(t-\tau, t-t_p)\,\mathrm{d}\tau \tag{4}$$

so that we no longer have a true convolution. In other words, following optical excitation, the material response is changing during traversal time of the THz probe pulse. A more complete

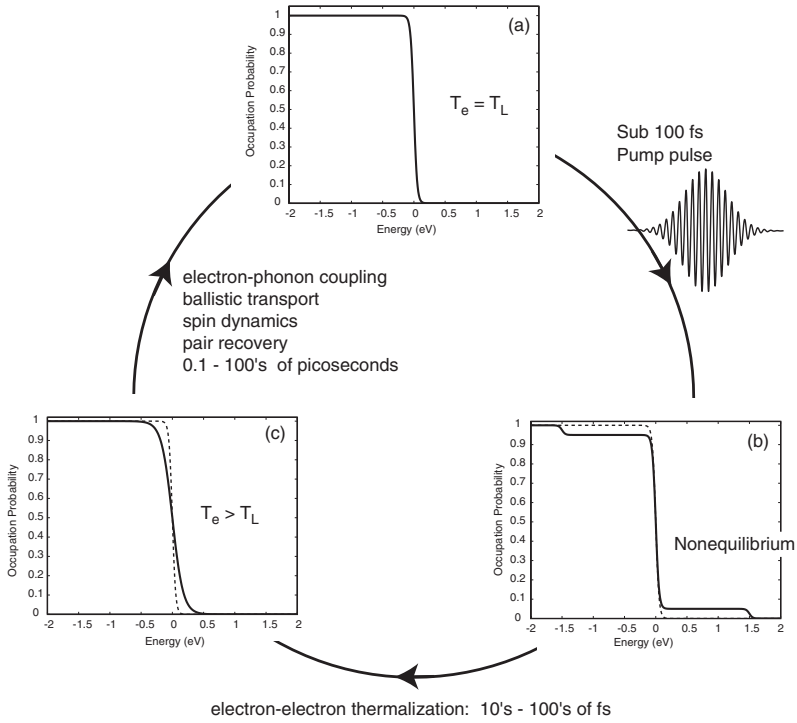

Figure 4. FD distribution in eqilibrium with $T_E = T_L$. (a), (b) A short optical pulse creates a nonthermal electron distribution. (b), (c) The nonthermal electron distribution thermalizes to a FD distribution through rapid e–e scattering resulting in $T_E > T_L$. Finally, in going from (c) to (a) the equlibrium is reestablished which in conventional metals occurs through e–p coupling followed by diffusion of excess phonons from the excitation region. In CEM, other degrees of freedom, such as spin, play a role in reequilibration. The dashed curves in (b) and (c) are of the initial distribution (a).

discussion of this problem can be found elsewhere (e.g. [33, 34], see especially [36]). Suffice to say, if the induced changes in the sample occur on a timescale comparable to or longer than the duration of the THz pulse, the prescription described above can provide considerable insight into the conductivity dynamics of the sample being studied. Finally, we note that this problem is not typically encountered in all-optical pump–probe spectroscopy since the spectral dependence is usually obtained experimentally and Fourier transform methods are not required.

3. Ultrafast dynamics in conventional metals

A useful starting point in understanding the utility of UOS in the study of CEMs is to consider the ultrafast dynamics of electrons in conventional metals [5–9]. In equilibrium, the electrons and lattice can be described by Fermi–Dirac (FD) and Bose–Einstein distributions respectively ($T_0 = T_E = T_L$, where T_E (T_L) is the electron (lattice) temperature and T_0 is the initial temperature). Since the lattice specific heat is much greater than the electronic specific heat ($C_L \gg C_E$), for a specific energy density deposited into a sample it is possible to drive the electrons out of equilibrium with respect to the lattice. A femtosecond pump pulse does this rapidly enough that the energy deposited in the electron distribution has not been transferred to the phonons. Thus, with a probe pulse it is possible to sensitively probe the energy relaxation

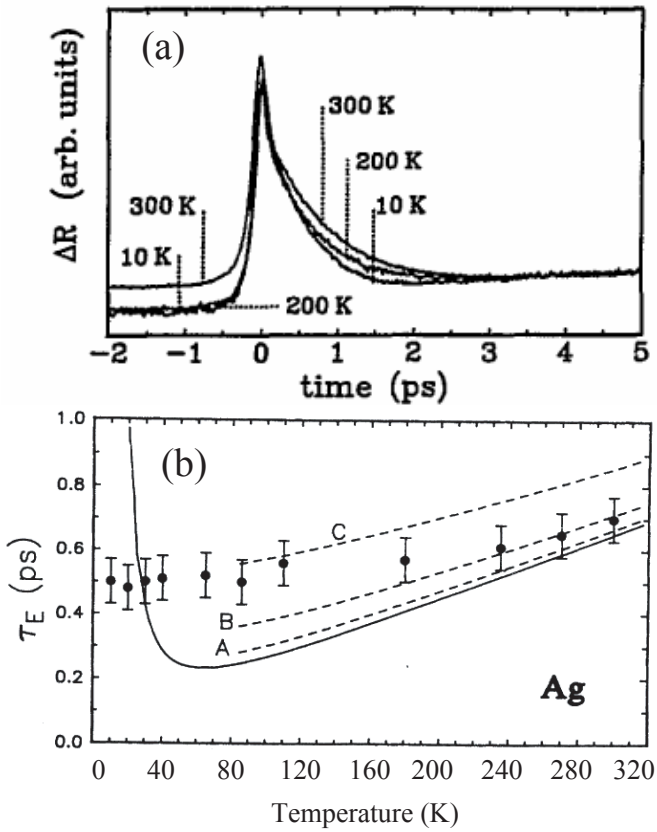

Figure 5. (a) Electron–phonon equilibration in an Ag thin film. (b) e–p equilibration as a function of temperature (data points). The solid curve is a calculation of e–p coupling using the TTM in the limit of depositing zero energy. The dashed curves are for nonzero energy densities—the disagreement between the data and the TTM is that the TTM neglects nonthermal effects (reproduced from [7] with permission).

of the excited electron distribution. For example, in Au and Cu, interband transitions (from the d band to the conduction band) have been used to probe changes in electron occupation near E_F. Figure 4 gives a basic description of the dynamics of electrons in metals in terms of changes in the occupation probability. Optical excitation with a short optical pulse creates a nonthermal distribution (see figure 4(b)) that rapidly (∼100 fs) thermalizes to an FD distribution through e–e scattering resulting in $T_E > T_L$ (note that e–e scattering cannot change the energy stored in the electron distribution). Subsequently, the sample returns to quasi-equilibrium (i.e. $T_E = T_L > T_0$) through e–p coupling and ballistic electron transport and finally returns to T_0 as the excess heat diffuses out of the excitation volume. As an example, figure 5(a) displays the ultrafast electron dynamics measured in a thin Ag film [7]. This exponential-like relaxation occurs primarily through electron–phonon coupling since the film is thin and the pump excitation is homogeneous across the thickness of the film. As figure 5(a) reveals, there is a slight decrease in the relaxation time with decreasing initial temperature.

The two-temperature model (TTM) has been extensively employed to describe the ultrafast electron dynamics in metals and goes a long way towards understanding figure 5 (as we shall see shortly, figure 5 also goes a long way towards understanding the limitations of the TTM

(full details can be found in [7]). The TTM is a set of coupled nonlinear differential equations that describe the temporal evolution of the energy density stored in the electron and lattice degrees of freedom [37].

$$C_E \frac{dT_E}{dt} = -G_{EL}(T_E - T_L) + \Xi(t) \tag{5}$$

$$C_L \frac{dT_L}{dt} = G_{EL}(T_E - T_L) - G_{SL}(T_L - T_S) \tag{6}$$

$$C_S \frac{dT_S}{dt} = G_{SL}(T_L - T_S). \tag{7}$$

In these equations, G_{EL} is the electron–phonon coupling function, $\Xi(t)$ is the deposited energy density from the optical pump pulse, C_S is the magnetic contribution to the specific heat and G_{SL} is the spin–lattice coupling function. The first two equations with $G_{SL} = 0$ constitute the TTM where we have neglected the the electronic and heat transport terms. For magnetic metals, the TTM can be extended to a three-temperature model (i.e. including equation (7) with $G_{SL} \neq 0$) which also describes the coupling of the lattice and spin degrees of freedom [38]. Ferromagnetic metals such as Fe and Co have recently been the subject of intensive investigation using UOS [38, 39], and as we will see this set of three coupled equations can be applied to the study of electron dynamics in the HMMs [40–42]. For now, we will continue the discussion in terms of the TTM.

There are of course many approximations that go into the TTM. First, the dynamics are described in terms of the energy density and changes in occupation are neglected. Perhaps most important of all is that the TTM assumes instantaneous thermalization to a FD distribution following optical excitation. That is, the TTM assumes T_E is well defined at all times and provides no insight into the e–e scattering that describes the evolution of the nonthermal electron distribution to a FD distribution (i.e. the dynamics in going from figure 4(a) to (b) are not considered). Nonetheless, the TTM has been very successful in describing the dynamics in metals. For low excitation fluence, the TTM equations can be linearized in that the temperature dependence of C_E, C_L and G_{EP} can be neglected since the change in the electronic temperature is small. In this case, the time for the electrons to equilibrate with the lattice is given by

$$\tau_{EL} = \frac{C_E C_L}{G_{EL}(C_E + C_L)}. \tag{8}$$

Since τ_{EL}, C_E and C_L can be experimentally measured, UOS is a powerful method to determine the electron–phonon coupling function G_{EL}. For example, in Ag and Au, the experimentally determined values are 3×10^{16} and 2×10^{16} W cm^{-3} s^{-1}. This compares favourably with theoretical estimates using

$$G_{EL} = \frac{\pi^2}{6} \frac{m s^2 n}{\tau} \tag{9}$$

where m is the electron mass, s is the sound velocity and τ is the electron collision time [43]. Figure 5(b) shows the temperature dependence of τ_{EL} as a function of temperature [7]. The solid curve is the prediction of the TTM in the limit of depositing zero energy into the sample and the dashed curves are for nonzero energy density. The point is that there are deviations in the temperature dependence between the experimental data and the TTM. As described in detail in [7]—see also [6, 9, 44–46], considering the initially created nonthermal electron distribution is a starting point in explaining the difference between the experimental data and the TTM. For example, for low excitation densities, the number of available final states for electron–electron scattering is small due to Pauli exclusion. Therefore, the initial nonthermal distribution can persist for some time following optical excitation. This means that there is a

smaller number of electrons emitting phonons than the simple TTM predicts and the nascent nonthermal electron distribution can increase the time it takes for the electrons to equilibrate with the lattice. These effects have been observed experimentally, but the full consequences of nonthermal electrons and e–e scattering at ultrafast timescales have not, to date, been elucidated either experimentally or theoretically.

In concluding this section we note that G_{EL} can be related to the electron–phonon coupling constant λ as shown by Allen [47]. Specifically, $\lambda\langle\omega^2\rangle = \pi k_b T_E G_{EL}/3\hbar$ where λ is the electron–phonon coupling constant and $\langle\omega^2\rangle$ is the second moment of the phonon spectrum. The experimental determination of λ using UOS for a variety of conventional metals and superconductors is in good agreement with other techniques [48]. Clearly, UOS has provided a great deal of insight into the dynamics of electrons in wide-band metals. In the next two sections we will see that UOS is sensitive to other degrees of freedom that are important in influencing or determining the electronic properties of CEMs.

4. Ultrafast dynamics in half-metallic manganites

It was during the 1950s that mixed valence manganite perovskites ($Re_{1-x}D_xMnO_3$, where Re is a rare earth such as La or Nd and D is a divalent alkali such as Sr or Ca) were first synthesized and extensively studied [49, 50]. For $x = 0.3$ a large negative magnetoresistance is observed near the Curie temperature T_C which coincides with the transition from paramagnetic semiconductor to ferromagnetic metal. Early on, this negative magnetoresistance (now commonly called colossal magnetoresistance (CMR) [19]) and corresponding metal–insulator transition was theoretically interpreted using a double-exchange model: electron transport between adjacent Mn ions via an intervening oxygen orbital is enhanced if the core spins on adjacent sites are parallel [51–53]. It is now realized that the double-exchange model alone cannot account for CMR behaviour since, for example, the magnitude of the resistivity in the paramagnetic phase is larger than spin scattering predicts [55, 56]. Coherent lattice effects such as the Jahn–Teller (JT) distortion of the MnO_6 octahedron that is static for the undoped parent compound and becomes dynamic with hole doping also affect the charge transport in the manganites. The simple picture is that in the paramagnetic phase the lattice distortion can follow the carriers from site to site since spin disorder reduces the kinetic energy of the carriers. This results in polaronic transport. Ferromagnetic ordering increases the carrier kinetic energy and the hopping from Mn to Mn is too rapid for the lattice distortion to follow although, as many studies have revealed, polaronic signatures persist below T_C. We refer the reader to the many reviews which describe the properties of the manganites in detail [56–63]. We also mention that the ground-state properties of manganites as a function of doping and temperature are an active area of research where the goal is to more fully understand the charge and orbitally ordered states and the origin of intrinsic mixed phases [62, 64]. However, in what follows we will emphasize the dynamics measured on the HMMs, specifically $La_{0.7}Ca_{0.3}MnO_3$ (LCMO, $T_C = 250$–270 K depending on the film quality), $La_{0.7}Sr_{0.3}MnO_3$ (LSMO, $T_C = 350$–360 K) and $Nd_{0.7}Sr_{0.3}MnO_3$ (NSMO, $T_C = 180$ K). Our emphasis is on these materials since, to date, ultrafast dynamics measurements on manganites at other dopings have not been performed (see [65] for a UOS study of $La_{0.82}Pb_{0.18}MnO_3$ and [66, 67] for studies of the ultrafast melting of the charge order in $Pr_{0.7}Ca_{0.3}MnO_3$ and $La_{0.5}Sr_{1.5}MnO_4$).

There have been numerous studies of the optical conductivity of HMMs (and manganites for other values of x as well) which show that as a function of decreasing temperature (or near T_C, as a function of magnetic field) a large shift of the spectral weight occurs [68, 70–72]. This spectral weight transfer (SWT) is intimately related to the CMR effect in dc conductivity measurements and involves the spin and lattice degrees of freedom. Figure 6

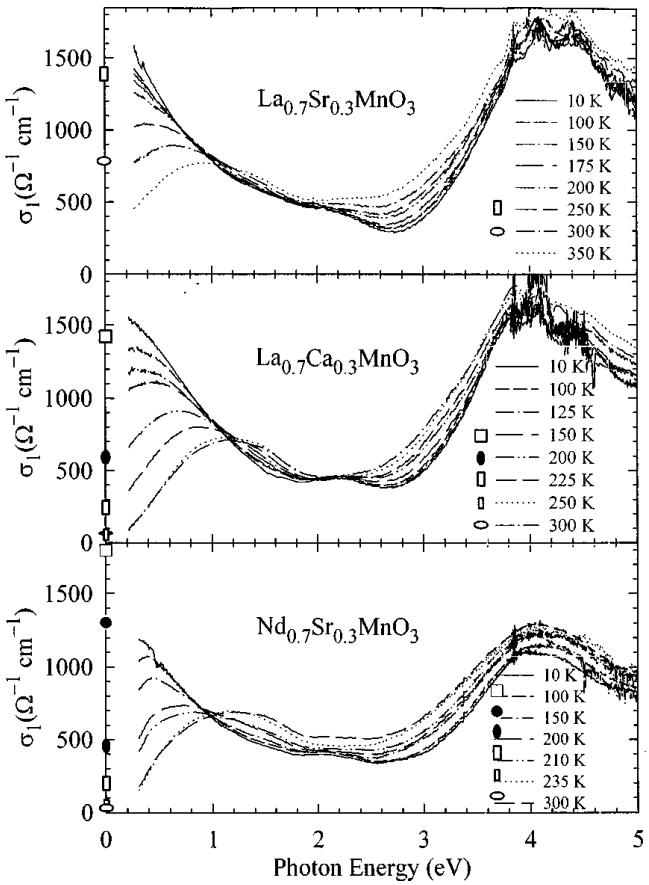

Figure 6. Optical conductivity versus energy for LCMO, LSMO and NSMO at various temperatures (reproduced from [68] with permission).

shows the temperature dependence of the optical conductivity from 0.2 to 5 eV as a function of temperature for three different samples [68]. This clearly shows the SWT with decreasing temperature and the development of a Drude peak centred at zero frequency. In [68], a detailed discussion of the features in the optical conductivity has been made and for all three HMMs in figure 6 the broad feature at $\sim$1.0 eV has been interpreted in terms of photon-induced hopping of JT polarons. With decreasing temperature it is the JT peak that evolves (partially) into a metallic response below T_C. This is just as discussed above in that, with increasing spin polarization, the increased carrier kinetic energy overcomes polaronic trapping of the carriers due to the JT distortion. The 3 eV feature has been ascribed to transitions between the spin-split e_g bands since, with decreasing temperature, this feature weakens in intensity (i.e. dipole-allowed transitions conserve spin so with increasing spin polarization this feature should weaken in strength—see especially figure 5 of [68]). Finally, the 4 eV peak is probably a charge transfer transition between the O_{2p} and Mn bands and shows little temperature dependence. Figure 7 shows the allowed transitions according to [68] where the transitions at 1 eV are (to be dipole allowed) interatomic transitons between d orbitals. In [69], however, it is claimed that intra-atomic transitions between d orbitals are permitted due to the strong hybridization between the Mn d orbitals and the O_{2p} orbitals.

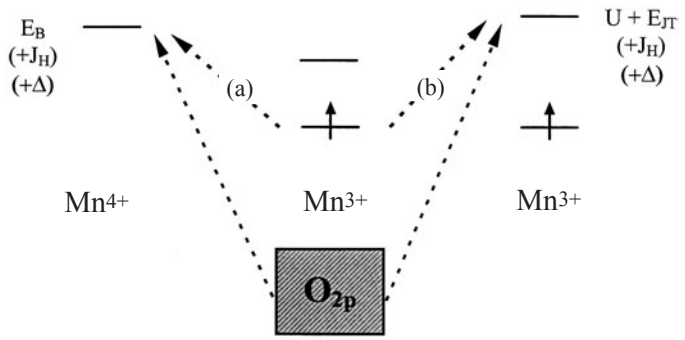

Figure 7. Optical transitions in manganites—e_g–e_g and O_{2p}–e_g transitions are displayed. We will focus on the Mn^{3+}–Mn^{4+} and Mn^{3+}–Mn^{3+} transitions labelled as (a) and (b) respectively. For (a) the energy of the transition is the breathing mode energy E_B plus the Hund's rule coupling energy J_H if the core spin of the Mn^{4+} is opposite to the e_g electron spin. For (b), it is the same except that an effective on-site Coulomb repulsion energy U must be included since the transition will result in a doubly occupied final state (reproduced in modified form from [68] with permission).

4.1. Quasiparticle dynamics: all-optical results

The brief introduction to the optical conductivity of the HMMs will help in understanding the results of the ultrafast optical dynamics. The results in this section and the next were obtained on epitaxial films prepared by pulsed laser deposition on $LaAlO_3$ (LAO) substrates using an XeCl excimer laser [73]. The films were excited and probed with 55 fs 1.5 eV pulses at 1 kHz at various temperatures above and below T_C. The pump and probe beams were both linearly polarized and orthogonal to each other.

The induced change in transmission for an LCMO film is plotted in figure 8(a) for different temperatures near T_C (270 K for this film) [40, 41]. The dynamics in figure 8(a) exhibit two components: an ultrafast (<1 ps) component and a much slower component (∼20–200 ps). In the following, we focus on the slow component. The component of interest is an induced decrease in transmission (increase in absorption) that develops below T_C. Figure 8(b) shows the dynamics measured at 280 K as a function of magnetic field. As the applied field is increased from 0 to 7 T, the dynamics are strongly modified and, with increasing spin order, look quite similar to the dynamics at lower temperatures as shown in figure 8(a), revealing that these dynamics are strongly influenced by the spin ordering. Figure 8(c) is a plot of the lifetime (triangles) as a function of temperature. At low temperatures the lifetime is approximately 20 ps and increases with increasing temperature to 260 ps at ∼250 K and then decreases. The lifetime as a function of applied field (circles) is also plotted using the conversion 280 K–8H where H is the magnetic field. Therefore, for this film, T_C is shifted by 8 KT^{-1}. Similar dynamics were also observed for LSMO (not shown) [40].

This slow component has been attributed to spin–lattice thermalization. The coupled differential equations (equations (5)–(7) above) can help to understand this. Optical excitation creates a nonthermal electron distribution that rapidly thermalized with the lattice on a picosecond timescale (this corresponds to the fast component in the dynamics). However, at this stage in the relaxation, the lattice and spins are not in equilibrium. Similar to the case for electron–phonon thermalization discussed previously, equations (6) and (7) describe the spin–lattice thermalization time

$$\tau_{SL} = \frac{C_S C_L}{G_{SL}(C_S + C_L)} \tag{10}$$

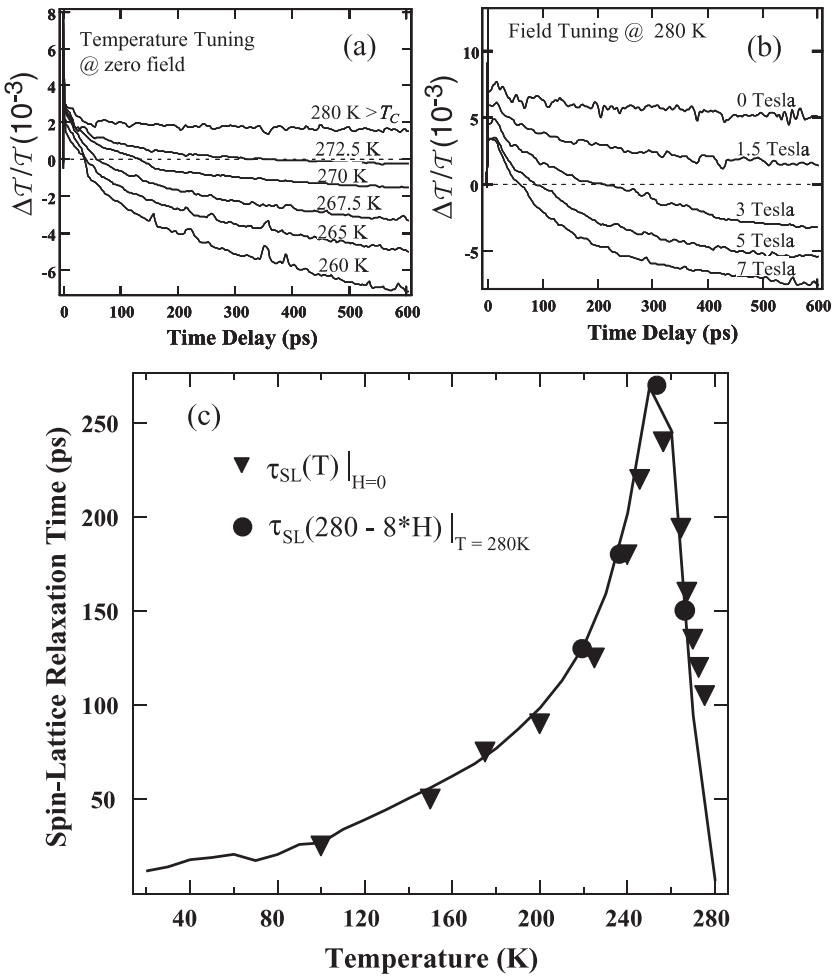

Figure 8. Optically induced change in transmission versus time at 1.5 eV for an LCMO thin film. (b) Magnetic field dependence of the induced transmission change. (c) Relaxation time versus temperature for the data in (a) and (b) (reproduced from [40, 41] with permission).

where G_{SL} is the spin–lattice coupling constant. Since $C_S < C_L$ this gives $\tau_{SL} \simeq C_S/G_{SL}$, showing that spin–lattice thermalization time is proportional to the magnetic specific heat. In [40], a mean field approximation was used to calculate the spin specific heat: $C_s = -\partial M^2/\partial T$. The curve in figure 8(c) shows the calculated C_s as a function of temperature scaled to fit the data. This demonstrates that the temperature dependence of the spin–lattice relaxation time in the critical region close to T_C originates from the magnetic specific heat and the fact that the spin–lattice energy coupling G_{SL} displays no strong temperature dependence. Microscopically, spin–lattice relaxation occurs through the coupling of spins to the anisotropic fluctuations of the crystal field produced by the phonons. This coupling is mediated by the spin–orbit interaction.

The dynamics in figure 8 were termed dynamic spectral weight transfer (DSWT) [40] since it is reasonable to expect that the transient temperature changes from the pump beam would result in a transfer of spectral weight similar to what is observed in the optical conductivity

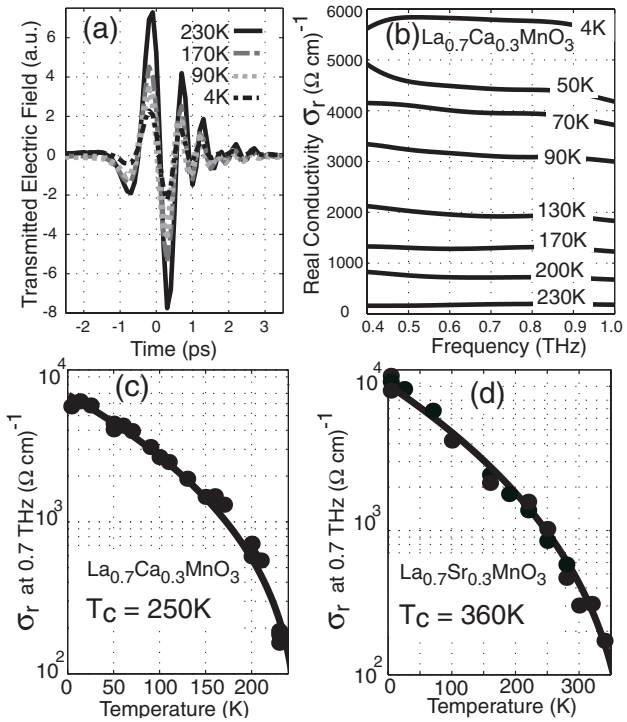

Figure 9. Temperature dependence of the THz transmission and real conductivity. (a) Transmitted electric field at various temperatures for a 90 nm thick LCMO film (see legend.) (b) Real conductivity versus frequency for LCMO at various temperatures. (c), (d) The value of the real conductivity at 0.7 THz as a function of temperature for LCMO and LSMO thin films. The lines are fits using equation (11) (reproduced from [42] with permission).

measurements shown in figure 6. In experiments where the dynamics were probed at 3.0 eV, no strong temperature dependence in the dynamics was observed in contrast to probing at 1.5 eV. Clearly then, spectral weight is not transferred between 1.5 and 3.0 eV. What would be more likely, as figure 6 suggests, is that upon photoexcitation DSWT would occur between the low energy Drude peak and the mid-IR peak near 1.0 eV. If this is the case, the induced increase in absorption measured at 1.5 eV (i.e. the data in figure 8) should be accompanied by a decrease in the conductivity in the far IR. In the next section, the similarity of the dynamics measured using OPTP to the all-optical data at 1.5 eV strongly supports this view.

4.2. Quasiparticle dynamics: far-infrared results

4.2.1. THz-TDS in HMMs. Before proceeding to the ultrafast conductivity dynamics measurements on HMMs, we will discuss the temperature dependence of the far-IR conductivity. This is one of the advantages of OPTP experiments in that the same set-up can be used for THz-TDS by simply blocking the optical pump beam. This provides a convenient method to help characterize a sample prior to dynamics measurements. Figure 9 shows THz-TDS results obtained on LCMO and LSMO films grown on LAO [42]. Figure 9(a) shows the THz electric field transmitted through an LCMO film at various temperatures without optical excitation. The magnitude decreases with decreasing temperature while the phase is

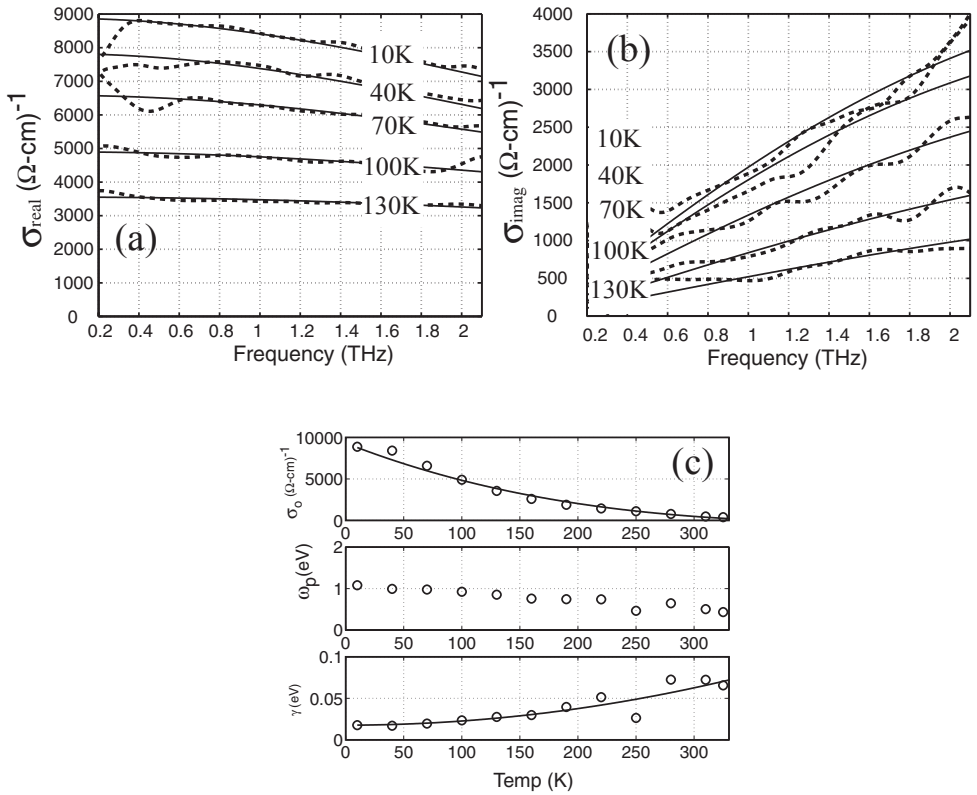

Figure 10. (a) σ_{real} and (b) σ_{imag} for an LSMO thin film on MgO. The dashed curves are the data and the solid curves are a best fit to the Drude model using equation (12). (c) Drude parameters versus temperature.

relatively constant. This indicates an increase in the real conductivity as the temperature is lowered. Figure 9(b) displays the real conductivity versus frequency for the LCMO film at various temperatures as determined from the data in figure 9(a) using equation (2). These conductivity measurements are in the regime $\omega\tau \ll 1$ (ω is the angular frequency and τ is the carrier collision time) as indicated by the flat frequency response. Figures 9(c) and (d) show the temperature dependence of σ_r at 0.7 THz for the LCMO and LSMO films respectively. The curves are fits to the conductivity using the following equation:

$$\sigma(T) = \sigma_o e^{M(T)/M_o} \tag{11}$$

where $M(T) \propto (1 - T/T_c)^{\beta} (\beta \simeq 0.33)$ is the magnetization and T_c is the transition temperature. These results are in reasonable agreement with DC resistivity measurements [74]. Figure 9(b) is a plot of the conductivity from 0.4 to 1.0 THz, whereas figure 3 shows that the THz bandwidth covers the range from 0.2 to 2.5 THz. The problem is that while LAO is an excellent substrate for growing epitaxial CMR films, it has twinning that strongly scatters radiation above 1 THz, making it difficult to reliably extract the conductivity over the full bandwidth of the THz pulse. This is not the case for films grown on MgO substrates. Figures 10(a) and (b) show $\sigma_1(\omega)$ and $\sigma_2(\omega)$ for LSMO on MgO. In this case the conductivity can be determined from 0.2

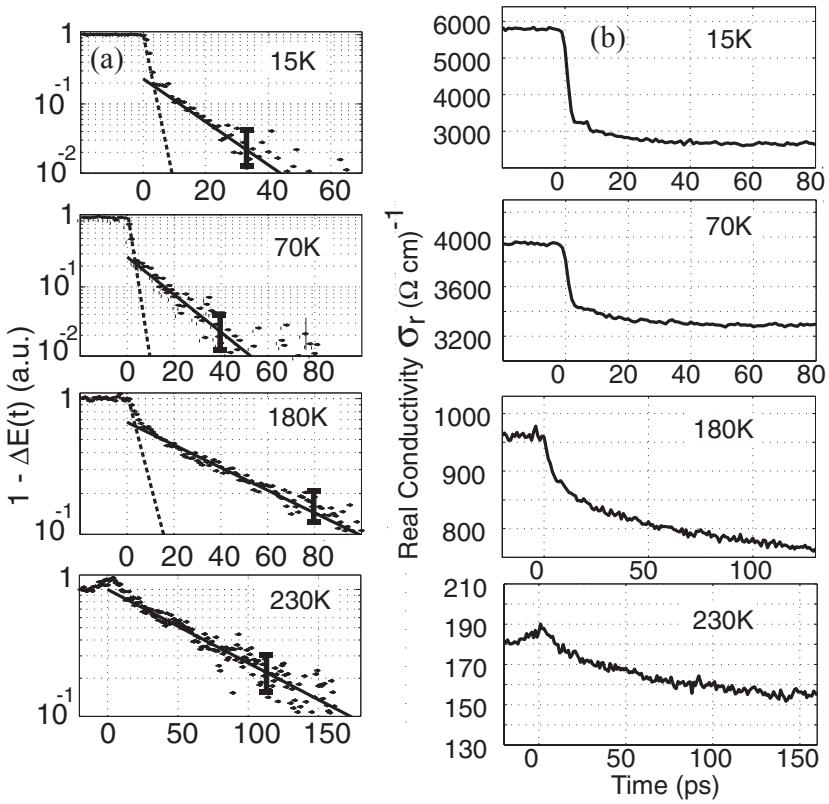

Figure 11. (a) One minus the induced change in electric field as a function of time for an LCMO film. (b) Corresponding change in the absolute conductivity (reproduced in modified form from [42] with permission).

to 2.0 THz which allows the data to be fitted using the Drude model for the conductivity:

$$\sigma(\omega) = \frac{\sigma_o}{\gamma - \mathrm{i}\omega} = \frac{\epsilon_0 \omega_p^2}{\gamma - \mathrm{i}\omega} \tag{12}$$

where ϵ_0 is free-space permittivity, ω_p is the plasma frequency and $\gamma = 1/\tau$ is the transport scattering rate. In figures 10(a) and (b), the dashed curves are the data and the solid curves are the Drude fits. Figure 10(c) shows the parameters obtained from the fits as a function of temperature. The results are in good agreement with other far-IR measurements on LCMO [75, 76]. Ultrafast conductivity measurements are ongoing for the HMM films on MgO. In the following section we will present the results obtained on HMM films grown on LAO.

4.2.2. Ultrafast conductivity dynamics in HMMs. In this section we review some of the results obtained from ultrafast conductivity measurements on HMMs using the experimental set-up depicted in figure 2. The data were collected using the one-dimensional scanning technique described earlier. Figure 11 show the dynamics for an LCMO film where in panel (a) $1 - \Delta E(t, t_p)$ is plotted (this is proportional to the conductivity change) as a function of t_p at different temperatures [42]. In panel (b) the same data are plotted in terms of the temporal changes in the absolute conductivity. Two components characterize the increase in

field transmission. There is a fast ∼2 ps component that is resolution limited. The data in figure 11 show that this component decreases in magnitude as the temperature is increased. The data also reveal a slow component that increases in relative magnitude as the temperature is increased. As the temperature is increased the lifetime of the slow component increases. These data are qualitatively similar to the all-optical data in figure 8. The fast component is due to a change in the conductivity as the electrons equilibrate with the lattice and the slower component is the spin–lattice relaxation described previously. The plateau in the conductivity at longer times corresponds to equilibrium between the electrons, spins and phonons, albeit at a higher temperature than before the arrival of the pump. On a nanosecond timescale the film recovers to the initial temperature as the phonons leave the film via thermal transport to the substrate.

Figure 12 shows τ_{SL} as a function of temperature for LCMO, LSMO and NSMO films. The same behaviour is observed as for the all-optical data, namely, τ_{SL} increases with temperature below T_C. The solid curves in figures 12(a) and (b) are calculations from numerically solving equations (5)–(7) using fits to the specific heat data of [77] (LCMO) and [78] (LSMO) (in figure 12(c) the solid curve is only to guide the eye). For these calculations, G_{SL} was assumed to be independent of temperature. The agreement between experiment and theory in figures 12(a) and (b) justifies this assumption yielding $G_{SL} = 2.5 \times 10^{15}$ (5×10^{15}) W m^{-3} K^{-1} for LCMO (LSMO). This numerical analysis further substantiates the simpler analysis used for the all-optical data and shows that τ_{SL} is proportional to the magnetic specific heat.

The results of this model can be extended to understand the induced change in conductivity ($\Delta\sigma$) as follows:

$$\Delta\sigma(t, T_L, T_S) = \frac{\partial\sigma}{\partial T_L}\Delta T_L(t) + \frac{\partial\sigma}{\partial T_S}\Delta T_S(t). \tag{13}$$

This equation shows that the temporal evolution of $\Delta\sigma$ depends on changes in the phonon $\Delta T_L(t)$ and spin $\Delta T_S(t)$ temperatures. It is important to have a measure of the relative importance of phonons and spins in determining σ. Such a measure is given by the quantity

$$\alpha \equiv \frac{\partial\sigma}{\partial T_S} \Big/ \frac{\partial\sigma}{\partial T_L}. \tag{14}$$

α is given by the ratio of the measured slow-component amplitude divided by the fast-component amplitude in the limit $C_S \ll C_L$. For temperatures less than ∼0.5 T_c(0.7 T_c) for LCMO (LSMO), α is smaller than one, indicating that phonons are the primary factor limiting hole transport in the e_g derived conduction band. In contrast, above these temperatures α is larger than one and continues to increase with temperature, indicating that spin fluctuations predominantly determine σ. For LSMO, $\alpha < 1$ occurs at ∼0.7 whereas for LCMO this occurs at ∼0.5 (see figure 3 of [42]). This is consistent with other measurements which indicate that polaronic behaviour persists to lower temperatures in LCMO than in LSMO.

The measured α places constraints on the dominant scattering mechanism. If holes were scattered primarily by thermally disordered ions, α would be small, as is observed at low temperatures. If they were scattered primarily by the simple double-exchange mechanism, α would be large, as is observed nearer to T_c. A more subtle case is a polaron/double-exchange scenario in which small polarons form only after the average hopping $\langle t \rangle$ is reduced due to local spin misalignment. Although phonons are involved in this scenario, they are phonons that coherently form a polaron (not thermally disordered phonons), and $\partial\sigma/\partial T_S$ dominates $\partial\sigma/\partial T_L$, resulting in a large α.

It is possible to use the experimental data to extrapolate the conductivity in the T_S–T_L plane by expanding $\ln(\sigma(T_s, T_L))$ in a power series and performing a least-squares fit using the data in figure 9 and the values for α. This has been accomplished for LCMO by expanding $\ln(\sigma)$ to third order in T_s and T_L. The results are shown in figure 13 as contours of constant $\ln(\sigma)$ in the

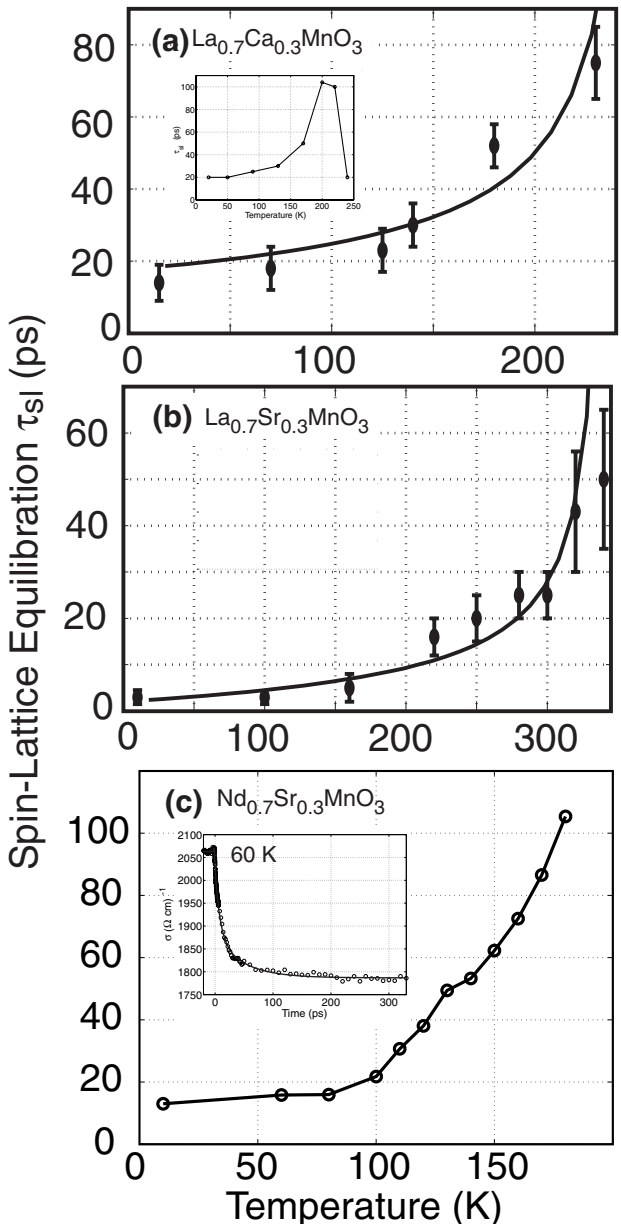

Figure 12. (a)–(c) Spin–lattice equilibration time for LCMO, LSMO and NSMO as a function of temperature. In (a) and (b) the solid curves are fits using equations (7)–(9) and described in the text. For (c) the curve is to guide the eye—the inset shows the measured dynamics at 60 K for NSMO. There is a two-component change as for the LCMO and LSMO films. ((a) and (b) reproduced in modified form from [42] with permission.)

T_S–T_L plane [42]. Conventional measurement techniques do not deviate from equilibrium as indicated by the white diagonal line. However, OPTP experiments, while starting from a point on the equilibrium line, allow for access to the portion of the T_S–T_L plane below the diagonal

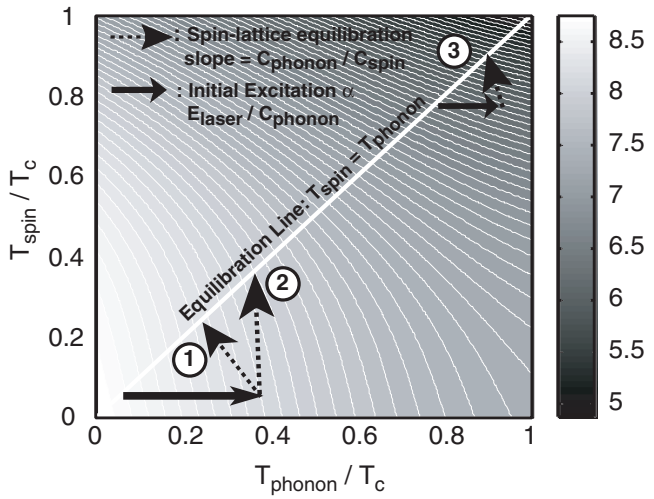

Figure 13. Contours of constant conductivity are plotted in the T_L–T_S plane (the greyscale bar is $\ln(\sigma)$). The curved white lines highlight the contours of constant conductivity. The arrows labelled 1–3 are discussed in the text (reproduced in modified form from [42] with permission).

equilibrium line since the excited electrons couple preferentially to the phonons during the initial 2 ps. This optically induced change in the phonon temperature is shown by the solid black arrow. The magnitude of this change is given by ξ/C_L where ξ is the deposited laser energy density. The system then returns to the equilibrium line as shown by the dashed arrows with the slope given by C_L/C_S. Depending on the initial temperature, ξ and $C_{L,S}$, the observed conductivity decrease can depend predominantly on T_L, T_S or both.

Figure 13 can be used to understand the dynamics shown in figure 11. The dynamics labelled by arrow 1 in figure 13 show a decrease in σ as the lattice temperature increases followed by a slight recovery in the conductivity upon approaching the equilibrium line. In this case the change in σ depends primarily on the phonon temperature. In figure 13 this is evident in that the contours of constant conductivity are nearly perpendicular to the phonon temperature axis. This is analogous to what is observed for LSMO. Arrow 2 in figure 13 again corresponds to a decrease in σ during the initial electron–phonon equilibration, followed by a further decrease in the conductivity as the spin temperature equilibrates with the lattice temperature. This two-component behaviour is observed in LCMO at low temperatures and indeed throughout most of the temperature range for LCMO, LSMO and NSMO up to higher initial temperatures where, as arrow 3 in figure 13 shows, the initial change in phonon temperature does not result in a large change in σ: the decrease is due mostly to spin fluctuations. This is evident in that the contours of constant conductivity are now nearly perpendicular to the spin temperature axis.

The ultrafast conductivity dynamics in LCMO and LSMO thin films show that $\partial\sigma/\partial T$ is determined primarily by thermally disordered phonons at low temperatures and by spin fluctuations at higher temperatures. Similar dynamics have now been observed in NSMO as well (see figure 12(c) and its inset).These data also confirm what was originally hypothesized for the all-optical data: the ultrafast dynamics can be viewed as DSWT between the low-energy Drude peak and the broad spectral feature at $\sim$1.0 eV in HMMs. These data also show that the lattice and spin degrees of freedom are both important in describing the dynamics of DSWT in the manganites.

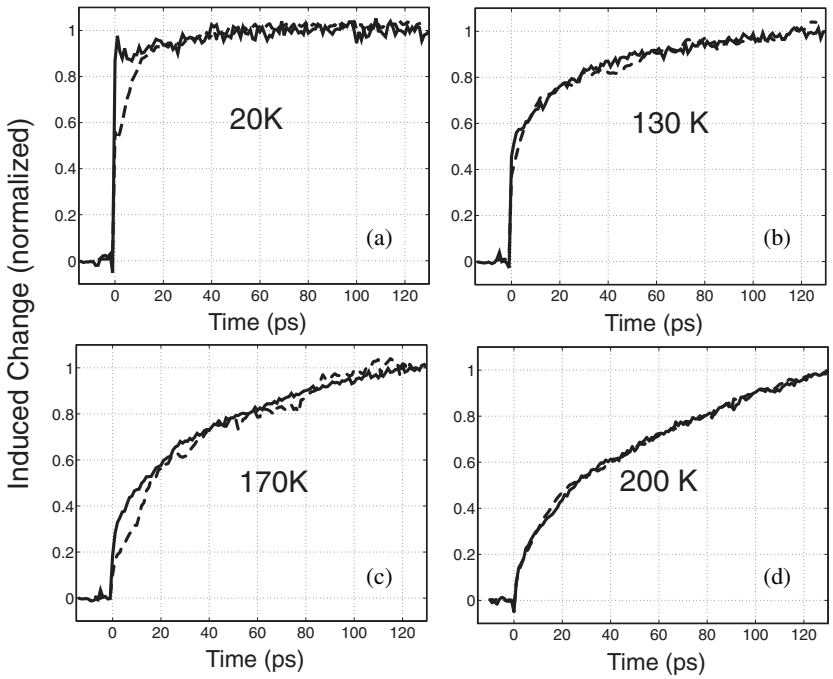

Figure 14. (a)–(d) Induced change in far-IR conductivity (solid curves) and reflectivity at 1.5 eV (dashed curves) for an LCMO thin film. The curves have been normalized to one to show the similarity in the data.

An important point regarding DSWT in the HMMs arises from comparing τ_{SL} obtained from all-optical measurements (figure 8(c)) and that obtained from OPTP measurements (figure 12(a)). The measured lifetimes are different in each case, and the question that arises is whether OPTP and all-optical techniques yield different values for τ_{SL}, or, more likely, if the the variation in the dynamics in different films is due to different growth conditions, impurity concentrations etc. To investigate this, we measured the dynamics on an LCMO film using OPTP, and then converted the set-up to all-optical induced reflectivity measurements at 1.5 eV without changing the pump beam so that the excitation conditions remained identical for both sets of measurements. Figure 14 shows the all-optical and OPTP measurements (normalized to unity) as a function of time at different temperatures. The solid curves are for the OPTP measurements and the dashed curves are the induced change in reflectivity at 1.5 eV. The excellent agreement between the two measurements clearly demonstrates that the two techniques measure the same τ_{SL}. These results suggest that a controlled study of how τ_{SL} varies with film growth conditions would potentially be interesting in understanding the properties of manganites, though difficult given the care required to grow high-quality epitaxial films. A study along these lines has recently been published [79].

The temperature dependence of τ_{SL} is suggestive of a diverging magnetic correlation length and the resultant critical slowing down of dynamics that can occur at a second-order phase transition. Such dynamics can exhibit universal behaviour, but the data shown here provide only a broad overview of the dynamics over a large temperature range. The measured τ_{SL} from these data does not show any characteristic power law behaviour suggestive of universal behaviour. To accomplish this, more careful measurements of τ_{SL} close to T_C would be required. Along these lines time-resolved magneto-optical Kerr rotation measurements in the half-metallic ferromagnet Sr_2FeMoO_6 have revealed critical dynamics [80]. Figure 15 shows the spin

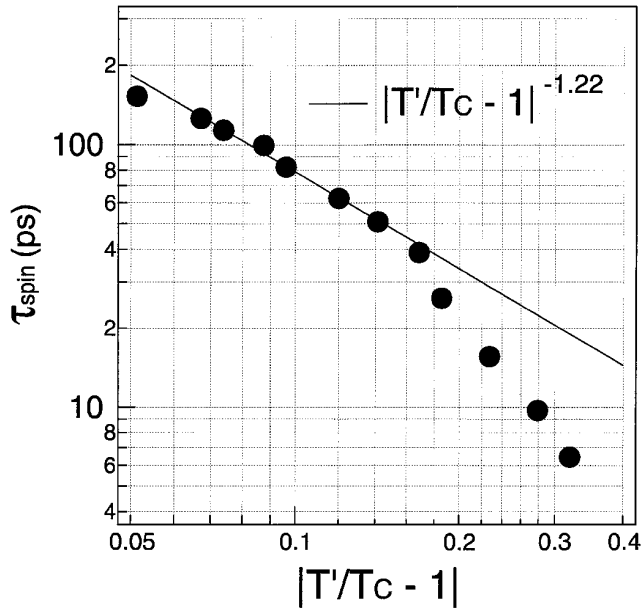

Figure 15. Spin–lattice relaxation time versus $|T/T_C - 1|$ for Sr_2FeMoO_6. The data show critical behaviour characteristic for a 3d spin system (reproduced from [80] with permission).

relaxation time as a function of temperature. From 0.8–1.0 T_C, the data can be fitted with $|T/T_C - 1|^{-z\nu} = |T/T_C - 1|^{-1.22}$ where z is the dynamic critical exponent and ν is the critical exponent for the correlation length. For the three-dimensional Ising model, $z\nu = 1.30$, and for the three-dimensional (two-dimensional) Heisenberg model $z\nu = 1.37(2.165)$ so figure 15 clearly shows that Sr_2FeMoO_6 is a three-dimensional spin system. Since the temperature dependence of the spin–lattice relaxation shows a power law behaviour, it should also be expected that the temporal dynamics would follow a power law. For example, the moment relaxation time is given as $M \sim (t)^{-\lambda}$ where $\lambda = \beta/z\nu$ with β the magnetization order parameter [81, 82]. Such an observation would probably require an extremely high signal-to-noise ratio to be experimentally observable. Finally, we mention that lower-temporal-resolution (i.e. nanosecond) optical methods have been used to investigate critical dynamics in the manganites [83].

5. Ultrafast dynamics in high-temperature superconductors

The origin of pairing in the copper oxide superconductors remains elusive in spite of ever increasing sophistication in the preparation and investigation of these materials [84]. The problem is so difficult that it is unlikely that a single experimental technique will provide an answer. Nonetheless, considerable progress has been made, and many experimental methods have contributed a great deal to the current understanding of HTSCs. This includes, to name a few, angle-resolved photoemission spectroscopy [85], tunneling experiments [86], neutron scattering [87] and microwave and optical conductivity measurements [88, 89]. The hope, as with these other experimental techniques, is that insights gained from UOS might help in understanding the normal state and superconducting properties of HTSCs.

There are several reasons which suggest that UOS can contribute to the understanding of the electronic properties of HTSCs. As the previous sections have shown, UOS can measure electron–phonon coupling in metals and is also sensitive to the spin degree of freedom. The successes of conventional optical spectroscopy as applied to HTSCs are many. This includes investigations of the condensation energy [90], relating the gap feature from optical spectroscopy at ∼50 meV to the 41 meV peak observed in neutron scattering [91], and measuring the quasiparticle and pair fractions in the superconducting state [15]. UOS can draw upon studies such as these with the dimension of time as an additional parameter that can be varied. Finally, the study of nonequilibrium effects in BCS superconductors has provided considerable insight into the interactions of quasiparticles and superconducting pairs which are intimately related to the superconducting order parameter [92, 93]. From this point of view, studies of nonequilibrium superconductivity in HTSCs have much, as we will see, to offer.

Early nonequilibrium studies of BCS superconductors showed that the time for quasiparticle recombination (τ_R) to Cooper pairs is sensitive to the magnitude of the superconducting gap Δ [94]. Close to T_C, $\tau_R \sim \tau_E/\Delta$ where τ_E is the inelastic scattering time and is dominated by the electron–phonon interaction. This predicts that close to T_C, τ_R diverges as $(1 - T/T_C)^{-1/2}$. However, experimentally measuring this intrinsic recombination time, as first noted in [95], is difficult since excited quasiparticle phonon emission (and the recombination process itself) leads to a distribution of phonons with energies greater than 2Δ. These phonons act as pair breakers and the decay time for the $>2\Delta$ phonons ($\tau_{2\Delta}$) is the rate limiting step for the observed pair recovery time $\tau_{\rm exp}$. In the limit of low density quasiparticle excitation, $\tau_{\rm exp}$ can still show a dependence on Δ (see e.g. equation (9) of [95]), and this has been observed in optically excited Al tunnel junctions [96]. More recent measurements using time-resolved far-IR spectroscopy have investigated pair breaking and pair recombination in Pb [26, 97]. In conventional superconductors, the small gap leads to long recovery times on the order of several hundred ps in (Pb) to hundreds of ns (Al). For HTSCs, the superconducting gaps are large in comparison to conventional superconductors and this necessitates the use of UOS to measure $\tau_{\rm exp}$.

5.1. HTSC quasiparticle/condensate dynamics: all-optical results

Initial studies using all-optical pump–probe spectroscopy on $YBa_2Cu_3O_{7-\delta}$ (YBCO) thin films revealed a response that changed dramatically at T_C showing, for example, a slow (bolometric) induced increase in $\Delta R/R$ above T_C crossing over to a fast induced decrease in $\Delta R/R$ below T_C [98, 99]. Below T_C, these data were interpreted in terms of a fast (i.e. 300 fs) avalanche process followed by quasiparticle recombination to Cooper pairs on a picosecond timescale limited by the 2Δ phonon relaxation time. More recent experiments have investigated this in detail [100, 101]. Photoinduced changes at 1.5 eV were performed on $Y_{1-x}Ca_xBa_2Cu_3O_{7-\delta}$ single crystals for $x = 0$ ($T_C = 93$ K) and $x = 0.132$ ($T_C = 75$ K). The left-hand panel of figure 16 shows the time dependence of $\Delta R/R$ for these samples [100]. With the y-axis plotted on a logarithmic scale, a two-exponent relaxation is clearly observable consisting of a fast (∼0.5 ps) and a slow (∼3 ps) component. The left-hand side shows both lifetimes plotted as a function of temperature for the four different crystals. The fast component is temperature independent while the slow component shows a quasi-divergence at T_C. This slow component was interpreted, as in [98], as the recombination time where $\tau_{\rm exp} \sim 1/\Delta$ with pair breaking due to phonons with energies greater than 2Δ limiting the recovery time. The fast component was associated with a temperature-independent gap (i.e. the pseudogap) and, being present at all dopings, suggests that the ground state is intrinsically spatially inhomogeneous. The amplitude dependence (see figure 3 of [100]) follows a BCS-like temperature dependence and

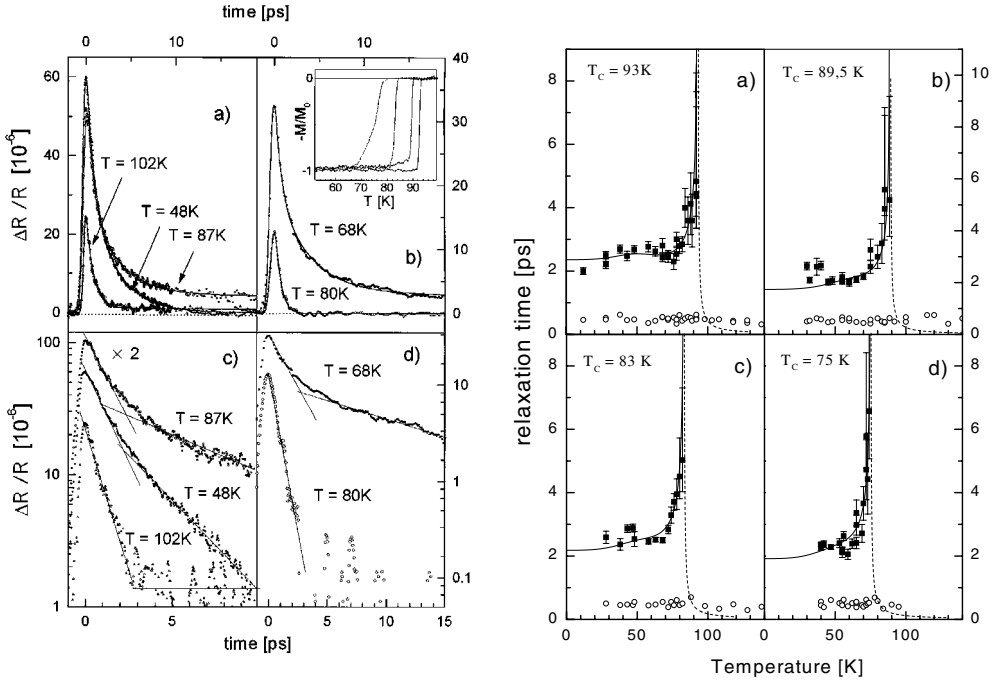

Figure 16. The right-hand panel shows the $\Delta R/R$ two-exponential dynamics for YBCO single crystals measured at 1.5 eV. The left-hand panel shows the corresponding relaxation times as a function of temperature. There is a clear divergence upon approaching T_C from below (reproduced from [100] with permission).

is inconsistent with a d-wave gap. This is in stark contrast with other measurements and may be related to pair recombination occurring away from the nodes of the gap. Alternatively, the d-wave nature may be averaged out since $\Delta R/R$ is averaged over the joint density of states. Most importantly, these results show that the recovery dynamics of $\Delta R/R$ are sensitive to the superconducting gap and pseudogap and that the reformation time of the condensate is rapid. Similar results on the charge density wave material $K_{0.3}MoO_3$ were obtained, showing that UOS measurements that probe the dynamics near E_F are quite sensitive to the opening of a gap in the DOS [102]. Ultrafast measurements of YBCO thin films in the mid-IR (60–200 meV) to directly probe the superconducting gap also revealed

(a) a picosecond recovery of the superconducting condensate,
(b) a subpicosecond response related to pseudogap correlations and
(c) a temperature dependence of the amplitude that follows the antiferromagnetic 41 meV peak observed in neutron scattering [103].

These dynamics are similar to the 1.5 eV measurements except for a difference in the temperature dependence of the amplitudes that remains unexplained.

Quite recently, a different interpretation for the $\Delta R/R$ dynamics measured on single-crystal samples of $YBa_2Cu_3O_{6.5}$ was put forward [104]. The data in this study revealed a $\Delta R/R$ recovery time that increases with decreasing fluence and increases with decreasing temperature. It is suggested that the recovery of $\Delta R/R$ is not due to quasiparticle recombination to the condensate, but rather is related to the thermalization of antinodal quasiparticles. They further suggested that the pair recovery should be much longer based in part on results obtained in [105]

(see [104] for the full details). In [106], similar behaviour was observed on Hg2212 and interpreted as a slowing down of the pair recovery due to a decreased probability for biparticle recombination. As we will see in the next section, using OPTP we can measure the dynamics of the quasiparticles and superconducting condensate simultaneously. The OPTP measurements directly show that the superconducting state has almost completely recovered in 10 ps, in reasonable agreement with [100], but in contradiction with the quasiparticle thermalization picture presented in [104].

5.2. Far-infrared dynamics in HTSCs

5.2.1. THz-TDS in HTSCs. As with the HMMs, by blocking the optical pump beam, it is possible to spectroscopically characterize an HTSC sample using THz-TDS. In fact, there have been many studies of the HTSCs using THz-TDS (and related far-IR and microwave techniques) that have provided significant insight into the electrodynamics [107–111] of HTSC materials. As representative examples, THz-TDS has been used to study the vanishing of phase coherence in $Bi_2Sr_2CaCu_2O_{8+\delta}$ (BSCCO) [107] and for the observation of the *c*-axis Josephson plasma resonance in $Tl_2Ba_2CaCu_2O_8$ [108, 109]. We will not review all of these measurements here and will instead focus on a few of the salient feature of the THz conductivity in HTSCs that are important in understanding the time-resolved conductivity results. The results presented in this section and the next were obtained on YBCO thin films grown on MgO substrates using pulsed laser deposition.

For the present discussion, the two-fluid model, which has been extensively used in describing the complex conductivity ($\sigma(\omega) = \sigma_1(\omega) + \mathrm{i}\sigma_2(\omega)$) in superconductors, will be employed [110, 113]. In this model, the conductivity is composed of two components: an imaginary component that is dominated, below T_C for the THz frequency range, by the superfluid population, and a Drude component that is proportional to the fraction of quasiparticles in the normal state. The two-fluid complex conductivity is given by

$$\sigma(\omega, T) = \frac{ne^2}{m^*}\left[\frac{f_n(T)}{\tau^{-1} - \mathrm{i}\omega} + f_s(T)\left(\frac{\mathrm{i}}{\omega} + \pi\delta(\omega)\right)\right] \tag{15}$$

where the first term corresponds to the normal fraction and the second term to the superconducting fraction. In this equation, n is the total carrier concentration, m^* is the effective mass, $f_n(T)$ and $f_s(T)$ are the normal and superconducting fractions ($f_n(T) + f_n(T) = 1$), respectively, τ ($=1/\gamma$—see equation (12)) is the transport scattering time and T is the temperature.

Figure 17 shows the measured conductivity (determined using equation (2)) for an optimally doped YBCO 50 nm thick film ($T_C = 89$ K) at (a) 60 K and (b) 95 K [112]. Similar data are shown for a $Y_{0.7}Pr_{0.3}Ba_2Cu_3O_7$ (YPBCO) 200 nm thick film ($T_C = 50$ K) at (c) 15 K and (d) 60 K. The plots are of $\sigma_2(\omega)(= \sigma_{im}(\omega))$ with the corresponding real conductivity $\sigma_1(\omega)(= \sigma_{re}(\omega))$ shown in the insets. For both the YBCO and YPBCO films, figures 17(b) and (d) show that above T_C, a simple Drude model (i.e. $f_n(T) = 1$) provides a reasonable fit to the data (at higher frequencies in the normal state, the optical conductivity does not go as $1/\omega^2$ as for a Drude model, but over the range of figure 17 a Drude fit is adequate). Now, at T_C long-range phase coherence is established and the quasiparticle fraction $f_n(T)$ becomes smaller than one. In the imaginary conductivity a characteristic $1/\omega$ frequency dependence results from the condensate fraction $f_s(T)$. This is clearly evident in both films as shown in figures 17(a) and (c). The solid black curves are the experimental data, and for the $\sigma_{im}(\omega)$ plots, the thin black curve is the quasiparticle conductivity, the short-dashed curve is the condensate conductivity and the long-dashed curve is the is the overall fit to the conductivity. The quasiparticle fraction

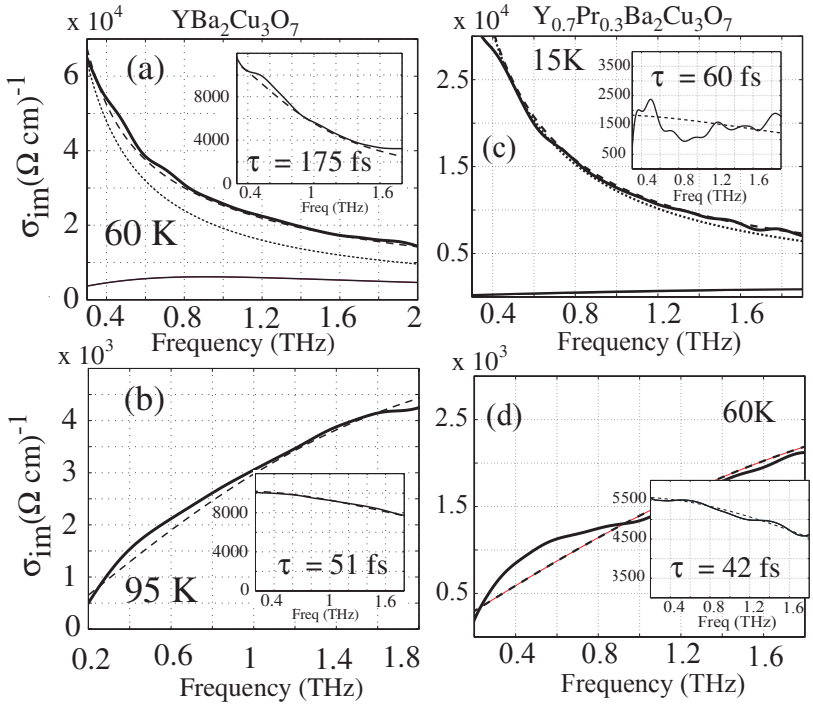

Figure 17. (a), (b) σ_{imag} (σ_{real} insets) for YBCO; (c), (d) YPBCO determined using equation (2). (a) and (c) are below T_C while (b) and (d) are above T_C. The fits were obtained using the two-fluid model (equation (15)) as described in the text ((a) and (b) reproduced with modifications from [112] with permission).

is independently obtained from fitting the real conductivity as shown in the insets. What is important in these data is that at temperatures somewhat below T_C, $\sigma_{im}(\omega)$ is dominated by the $1/\omega$ condensate fraction though there is a nonzero quasiparticle fraction as well.

In figure 18, the values of $f_n(T)$, $f_s(T)$ and τ are plotted as a function of temperature for a YBCO film (different than the one for which the data are plotted in figure 17) and the YPBCO film (the same film as in figures 17(c) and (d)). With decreasing temperature, $f_n(T)$ ($f_s(T)$) decreases (increases) as more quasiparticles are transferred to the condensate. In addition, the transport scattering time increases, eventually saturating due to impurity scattering. The temperature dependence of $\sigma_{re}(\omega)$ for these films (not shown) [33] goes as $1 - (T/T_C)^2$ which is what is expected for d-wave paring with impurity scattering (although it is not clear why this is commonly observed in thin films over such a large temperature range [113]). As figure 18 shows, this simple two-fluid analysis does not account for the entire Drude spectral weight. For the YBCO film $f_n(T) + f_s(T) \simeq 0.9$ at all temperatures below T_C, and for the YPBCO $f_n(T) + f_n(T) \simeq 0.8$ below T_C. This may be related to order parameter fluctuations which draw spectral weight from the condensate as observed in BSCCO thin films [114]. Nonetheless, figures 17 and 18 show that the two-fluid model provides a reasonable first-order description of the THz conductivity in YBCO and YPBCO films. What is most important for the interpretation of the OPTP measurements presented in the next section is that $\sigma_{re}(\omega)$ is due entirely to quasiparticles and $\sigma_{im}(\omega)$ is dominated by the condensate.

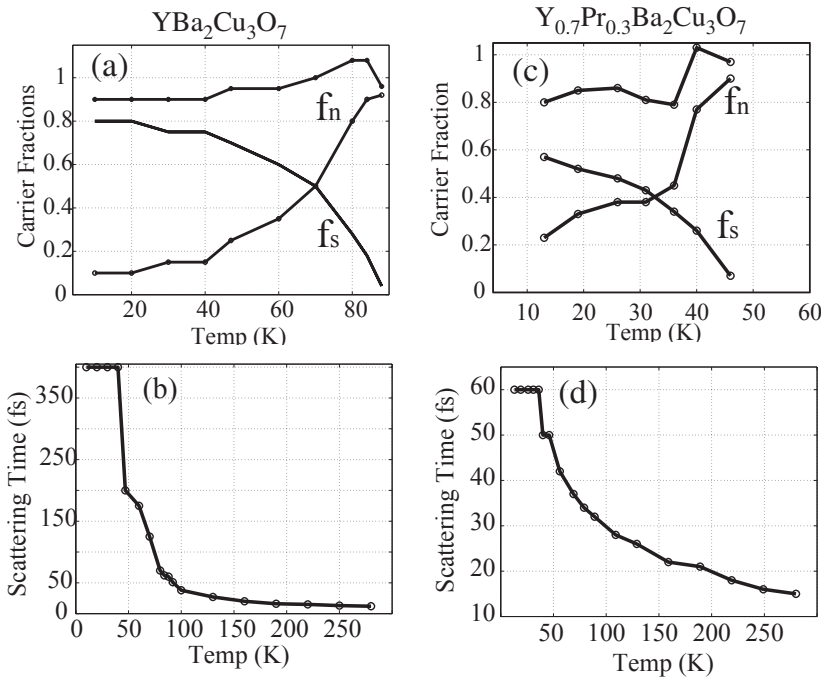

Figure 18. (a), (c) Quasiparticle (f_n) and superconducting (f_n) fractions as a function of temperature for YBCO and YPBCO films, respectively. (b), (d) The transport scttering times as a function of temperature for a fit to equation (15) which reduces to the Drude model above T_C.

5.2.2. Ultrafast conductivity dynamics in HTSCs. As with the all-optical dynamics, photoexcitation results in a distribution of quasiparticles that, in an avalanche process, break Cooper pairs resulting in an increase in the number of quasiparticles and a decrease in the superconducting pair fraction. Subsequently, pair recovery occurs. With OPTP, however, it is possible to directly observe the ground-state recovery through monitoring the induced changes in the THz conductivity. Initial experiments showed that the THz conductivity recovered on a ps timescale, but these measurements were performed at a fairly high fluence in which the system was almost driven normal [115]. Even at these high fluences ($\sim$100 μJ cm^{-2}), there was a increase in the pair recovery time (in this section we will denote this as τ_σ) for an optimally doped film upon approaching T_C. These data are shown as the solid circles in figure 20(a) and are quite similar to the all-optical results in the left-hand panel of figure 16. For a $YBaCuO_{6.5}$ film ($T_C = 50$ K) the lifetime is temperature independent (solid triangles in figure 20(a)) up to T_C and is consistent with the presence of a pseudogap. This is again similar to all-optical measurements though the lifetime from OPTP is 3 ps whereas for the all-optical dynamics the temperature-independent lifetime is approximately 0.5 ps.

Improvements in the sensitivity of OPTP have enabled ultrafast dynamics measurements on YBCO thin films [112] to be performed at fluences approximately one order of magnitude less (i.e. $\sim$10 μJ cm^{-2}) than in [115]. In the following, we briefly present the results of these experiments which were performed on the films whose conductivity is plotted in figure 17. For the YBCO film, $\sigma_{im}(\omega)$ ($T = 60$ K) as a function of frequency at various times following optical excitation is shown in figure 19(a). Figure 19(c) shows similar data though for the YPBCO film at 25 K. For both films, at 1 ps after optical excitation there is a decrease in the imaginary conductivity corresponding to a decrease in the condensate fraction (note

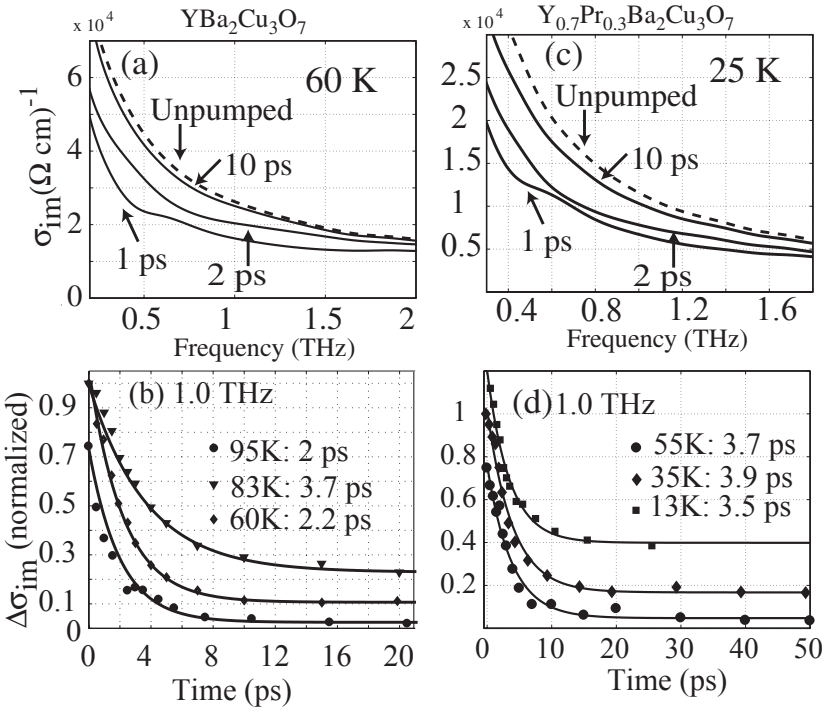

Figure 19. (a), (c) The imaginary conductivity as a function of frequency at various times following photoexcitation for YBCO and YPBCO. Clearly, the $1/\omega$ condensate fraction recovers on a picosecond timescale. (b), (d) The recovery dynamics of the imaginary conductivity at 1.0 THz at different temperatures (the curves are offset vertically for clarity). ((a) and (b) reproduced with modifications from [112] with permission.)

however that the $1/\omega$ is still observable, indicating a nonzero $f_s(T)$). This decrease rapidly recovers on a ps timescale, and since $\sigma_{im}(\omega)$ is being measured, must be due, in large part, to superconducting pair reformation (see below, however). In particular, these data clearly show that the superconducting state has almost completely recovered 10 ps after optical excitation.

Figures 19(b) and (d) plot the induced change in $\sigma_{im}(\omega)$ at 1.0 THz at several temperatures for the YBCO and YPBCO films, respectively (the curves are displaced vertically for clarity). The solid curves are best fits to the data. For the YBCO film, as in the previous higher-fluence study and the all-optical studies, the lifetime increases upon approaching T_C. The recovery time at 95 K is 2 ps, and at this temperature is no longer a measure of the pair recovery but is probably due to electron–phonon equilibration. For the YPBCO film the lifetime is relatively constant at approximately 3.5 ps, even above T_C. This, again, is suggestive of the presence of a pseudogap in this underdoped material. Figure 20(a) shows the lifetimes from figure 19(b) and (d) plotted as open symbols along with the data from [115]. The agreement is quite good with the higher-fluence measurements on different films. In particular, the dynamics for the underdoped $YBa_2Cu_3O_{6.5}$ film and the YPBCO film have the same lifetime and show no temperature dependence.

Finally, figure 20(b) is a plot of the induced change in $\sigma_{im}(\omega)$ for the YBCO film as a function of time at different frequencies [112]. With increasing frequency, the recovery of $\sigma_{im}(\omega)$ is faster. In the limit of zero quasiparticle fraction, this induced change would be solely due to superconducting pair recovery. However, there are quasiparticles present (at 60 K the initial

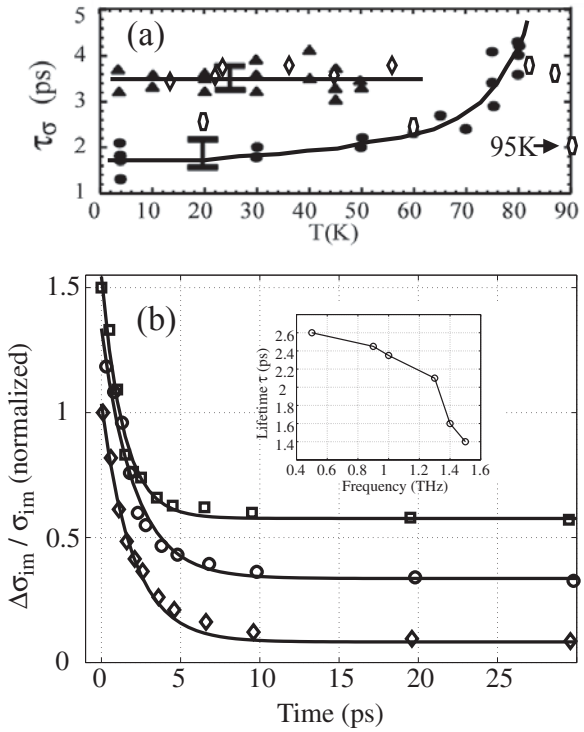

Figure 20. (a) Measured condensate recovery time for (▲) $YBa_2Cu_3O_{6.5}$ and (◇) YPBCO thin films both of which have $T_C = 50$ K. (●), (○) recovery dynamics for $YBa_2Cu_3O_7$ films with $T_C = 85$ and 89 K respectively. An increase in the lifetime occurs close to T_C. (b) Normalized induced change in the imaginary conductivity (60 K) as a function of time at various frequencies. The curves are displaced vertically for clarity. The solid curves are fits to the function $y = a \times \exp(-t/\tau_\sigma) + b$. The inset shows the measured lifetime as a function of frequency. ((a) reproduced with modifications from [115] and (b) reproduced from [112] with permission.)

quasiparticle fraction is ∼40%) so the quasiparticle fraction makes a non-negligible contribution to $\sigma_{im}(\omega)$. At higher frequencies this fraction becomes increasingly important since the superconducting pair fraction response goes as $1/\omega$. This offers a potential explanation for the decrease in the lifetime of the $\sigma_{im}(\omega)$ recovery with increasing frequency: at low frequencies $\sigma_{im}(\omega)$ is dominated by superconducting pair recovery, but at higher frequencies the relaxation is increasingly influenced by an additional relaxation pathway associated with the quasiparticles. This is further supported in that the recovery of $\sigma_{re}(\omega)$ is quite short (∼1.5 ps independent of frequency). Speculating on the origin of this additional relaxation pathway, it could be due to the relaxation of the excited quasiparticles into the nodes of the superconducting gap along $k_x = k_y$. Since this process is faster than the superconducting pair recovery, this suggests that the excited quasiparticles relax into the nodes of the gap followed by pair recovery.

6. Conclusions and future directions

In the previous two sections it has been demonstrated that UOS can probe the dynamics of correlated electrons. In the HMM, below the Curie temperature, OPTP experiments show that thermally disordered phonons limit the conductivity at low temperatures and that spin

disorder becomes increasingly important close to T_C. The all-optical experiments show the same dynamics as the OPTP experiments. This provides a surprisingly consistent picture in which the dynamic measurements probe the degrees of freedom responsible for the large spectral weight shifts in the optical conductivity. For the HTSCs, the temperature dependence of the dynamics is very sensitive to the opening of the gap—this is quite general and has been observed in CDW materials as well. The superconducting condensate recovers on a picosecond timescale as directly observed using OPTP. This is in good agreement with the more indirect all-optical measurements at 1.5 eV. The similarity between the OPTP and all optical dynamics in both of these systems shows that all-optical UOS can sensitively probe the dynamics of quasiparticles near E_F and that OPTP directly probes the degrees of freedom limit or enhanced charge transport.

The examples presented here only begin to elucidate the utility of UOS in the study of CEMs. For example, OPTP has become sensitive enough to measure changes in the conductivity in the paramagnetic semiconducting phase of the manganites. Preliminary results show that the dynamics which originate in the paramagnetic phase persist into the ferromagnetic phase, offering the possibility to probe the dynamics in intrinsic mixed phases [116]. It may, for example, also be possible to measure polaron formation times in the manganites. We have emphasized the dynamics in HMMs, but, of course, UOS dynamics measured as a function of doping with a divalent substituent should permit dynamic measurements of charge and orbitally ordered states. Similarly, some ultrafast measurements of the dynamics in HTSCs as a function of doping have been performed, but clearly a great deal more can be learned with further studies along these lines. There are entire classes of CEM (or CEM-like) materials which are interesting candidates for UOS studies. For example, measuring the ultrafast dynamics in other compounds that display a large negative magnetoresistance near the Curie temperature (such as EuO, EuB_6 or $Tl_2Mn_2O_7$) might help clear up the apparently differing origin of CMR in these materials. As another example, recent measurements on heavy-fermion single crystals (e.g. $YbInCu_4$) show that the e–p equilibration time increases dramatically below the Kondo temperature T_K [117]. Such experiments may help determine whether the electronic ground state is a many-body Kondo state that forms only below T_K, or is more simply described in terms of the thermal population of a narrow-gap system with the gap arising from hybridization between the conduction electrons and localized f electrons. Finally, we mention the idea of investigating critical dynamics at a second-order phase transition as briefly discussed above with regard to Sr_2FeMoO_6 [80]. Attempting to observe and determine universal dynamics across classes of materials would be seem to be a worthwhile pursuit.

In this review we have emphasized two ultrafast optical techniques in probing quasiparticle dynamics in CEMs. There are other ultrafast techniques that should be considered as well. Time-resolved magneto-optical Kerr spectroscopy is a direct probe of the magnetization dynamics and would seem to offer great potential in investigating CEMs (as for Sr_2FeMoO_6). Another exciting method is ultrafast x-ray diffraction where an optical pulse induces a change in a sample and a subpicosecond x-ray pulse monitors the induced change in the structure [118]. For example, an ultrafast nonthermal solid–solid phase transition in VO_2 [119] has been observed using this technique. Experiments such as this where higher pump fluences are used to drive a phase transition may provide insight into the nature of the metal–insulator transition in CEMs.

Optical conductivity measurements as a function of photon energy, temperature and magnetic field have proven to be a powerful method in helping unravel the relative importance of charge, lattice, spin and orbital degrees of freedom in CEMs. We hope this brief review has demonstrated that UOS is a powerful technique that complements conventional optical techniques in understanding the properties of CEMs.

Acknowledgments

There have been many contributors to the work presented in this article. We would especially like to thank C Kwon and Q X Jia for providing high-quality epitaxial films. In addition, we would like to thank S A Trugman, A I Lobad and V K Thorsmølle, for making important contributions to much of this work, and J Demsar for insightful discussions. We would also like to thank our colleagues whose results are included in this review for their permission to present their work. Research supported by the Los Alamos Laboratory Directed Research and Development Program, Department of Energy.

References

[1] See, for example
Elsaesser T, Mukamel S, Murnane M M and Scherer N F (ed) 2001 *Ultrafast Phenomena* vol 12 (Berlin: Springer)
[2] Shah J 1999 *Ultrafast Spectroscopy of Semiconductors and Semiconductor Nanostructures* (New York: Springer)
[3] Chemla D S and Shah J 2001 *Nature* **411** 549
[4] Huber R, Tauser F, Brodschelm A, Bichler M, Abstreiter G and Leitenstorfer A 2001 *Nature* **414** 286
[5] Eesley G L 1983 *Phys. Rev. Lett.* **51** 2140
[6] Fann W S, Storz R, Tom H W K and Borkor J 1992 *Phys. Rev. Lett.* **68** 2834
[7] Groeneveld R H M, Sprik R and Lagendijk A 1995 *Phys. Rev.* B **51** 11433
[8] Schoenlein R W, Lin W Z, Fujimoto J G and Eesley G L 1987 *Phys. Rev. Lett.* **58** 1680
[9] Sun C K, Vallee F, Acioli L H, Ippen E P and Fujimoto J G 1994 *Phys. Rev.* B **50** 15337
[10] Spence D E, Kean P N and Sibbett W 1991 *Opt. Lett.* **16** 42
[11] Maine P, Strickland D, Bado P, Pessot M and Mourou G 1988 *IEEE J. Quantum Electron.* **24** 398
[12] Grischkowsky D, Keiding S, VanExeter M and Fattinger C 1990 *J. Opt. Soc. Am.* B **7** 2006
[13] Wu Q and Zhang X C 1995 *Appl. Phys. Lett.* **67** 3523
[14] Nahata A, Weling A S and Heinz T F 1996 *Appl. Phys. Lett.* **69** 2321
[15] Nuss M C, Mankiewich P M, Omalley M L, Westerwick E H and Littlewood P B 1991 *Phys. Rev. Lett.* **66** 3305
[16] Harde H, Cheville R A and Grischkowsky D 1997 *J. Phys. Chem.* A **101** 3646
[17] Mittleman D M, Jacobson R H and Nuss M C 1996 *IEEE J. Sel. Top. Quantum Electron.* **2** 679
[18] Bednorz J G and Muller K A 1986 *Z. Phys.* B **64** 189
[19] Jin S, Tiefel T H, McCormack M, Fastnacht R A, Ramesh R and Chen L H 1994 *Science* **264** 413
[20] Allen J W, Aronson M, Boebinger G S, Broholm C L, Cooper S L, Crow J E, Hammel P C and Lander G 2002 *Physica* B **318** 12
[21] Nuss M C and Orenstein J 1998 *Millimeter and Submillimeter Wave Spectroscopy of Solids* ed G Grüner (Berlin: Springer)
[22] Grischkowsky D 1993 *Frontiers in Nonlinear Optics* ed H Walther, N Koroteev and M O Scully (Philadelphia, PA: Institute of Physics Publishing)
[23] Nahata A, Cao H and Heinz T F 2002 *IEEE Circuits Devices* **18** 32
[24] Huber R, Brodschelm A, Tauser F and Leitenstorfer A 2000 *Appl. Phys. Lett.* **76** 3191
[25] Kono S, Tani M, Gu P and Sakai K 2000 *Appl. Phys. Lett.* **77** 4104
[26] Federici J F, Greene B I, Saeta P N, Dykarr D R, Sharifi F and Dynes R C 1992 *Phys. Rev.* B **46** 11153
[27] Groeneveld R H M and Grischkowsky D 1994 *J. Opt. Soc. Am.* B **11** 2502
[28] Prabhu S S, Ralph S E, Melloch M R and Harmon E S 1997 *Appl. Phys. Lett.* **70** 2419
[29] Beard M C, Turner G M and Schmuttenmaer C A 2001 *J. Appl. Phys.* **90** 5915
[30] Schall M and Jepsen P U 2000 *Opt. Lett.* **25** 13
[31] Liu K P H and Hegmann F A 2001 *Appl. Phys. Lett.* **78** 3478
[32] Knoesel E, Bonn M, Shan J and Heinz T F 2001 *Phys. Rev. Lett.* **86** 340
[33] Averitt R D, Rodriguez G, Siders J L W, Trugman S A and Taylor A J 2000 *J. Opt. Soc. Am.* B **17** 327
[34] Kindt J T and Schmuttenmaer C A 1999 *J. Chem. Phys.* **110** 8589
[35] Beard M C and Schmuttenmaer C A 2001 *J. Chem. Phys.* **114** 2903
[36] Němec H, Kadlec F and Kužel P 2002 *J. Chem. Phys.* **117** 8454

[37] Anisimov S I, Kapeliovich B L and Perel'man T L 1974 *Zh. Eksp. Teor. Fiz.* **66** 776–81 (Engl. transl. 1974 *Sov. Phys.–JETP* **39** 375–7)
[38] Beaurepaire E *et al* 1996 *Phys. Rev. Lett.* **76** 4250
[39] Koopmans B *et al* 2000 *Phys. Rev. Lett.* **85** 844
[40] Lobad A I, Averitt R D, Kwon C and Taylor A J 2000 *Appl. Phys. Lett.* **77** 4025
[41] Lobad A I, Averitt R D and Taylor A J 2001 *Phys. Rev.* B **63** 060410(R)
[42] Averitt R D, Lobad A I, Kwon C, Trugman S A, Thorsmølle V K and Taylor A J 2001 *Phys. Rev. Lett.* **87** 017401
[43] Kaganov M I, Lifshitz I M and Tanatarov L V 1956 Relaxation between electrons and the crystalline lattice *Zh. Eksp. Teor. Fiz.* **31** 232–7 (Engl. transl. 1957 *Sov. Phys.–JETP* **4** 173–8)
[44] Bejan D and Raseev G 1997 *Phys. Rev.* B **55** 4250
[45] Gusev V E and Wright O B 1998 *Phys. Rev.* B **57** 2878
[46] Lugovskoy A V and Bray I 1999 *Phys. Rev.* B **60** 3279
[47] Allen P B 1987 *Phys. Rev. Lett.* **59** 1460
[48] Brorson S D, Kazeroonian A, Moodera J S, Face D W, Cheng T K, Ippen E P, Dresselhaus M S and Dresselhaus G 1990 *Phys. Rev. Lett.* **64** 2171
[49] Jonker G H and van Santen J H 1950 *Physica* **16** 337
[50] Volger J 1954 *Physica* **20** 49
[51] Anderson P W and Hasegawa H 1955 *Phys. Rev.* **100** 67
[52] de Gennes P-G 1960 *Phys. Rev.* **118** 141
[53] Kubo K and Ohata N 1972 *J. Phys. Soc. Japan* **33** 21
[54] Millis A J, Littlewood P B and Shraiman B I 1996 *Phys. Rev.* B **54** 5405
[55] Roder H, Zhang J and Bishop A R 1996 *Phys. Rev. Lett.* **76** 1356
[56] Millis A J 1998 *Nature* **392** 147
[57] Ramirez A 1997 *J. Phys.: Condens. Matter* **9** 8171
[58] Coey J M D, Viret M and von Molnar S 1999 *Adv. Phys.* **48** 167
[59] Salamon M B and Jaime M 2001 *Rev. Mod. Phys.* **73** 583
[60] Nagaev E L 2001 *Phys. Rep.* **346** 387
[61] Tokura Y (ed) 2000 *Colossal Magnetoresistive Oxides* (Amsterdam: Gordon and Breach)
[62] Dagotto E, Hotta T and Moreo A 2001 *Phys. Rep.* **344** 1
[63] Imada M, Fujimori A and Tokura Y 1998 *Rev. Mod. Phys.* **70** 1039
[64] Saiyoh E, Okamoto S, Takahashi K T, Tobe K, Yamamoto K, Kimura T, Ishihara S, Maekawa S and Tokura Y 2001 *Nature* **410** 180
[65] Mertelj T, Bosak A A, Gorbenko O Y, Kaul A R and Mihailovic D 2000 *Int. J. Mod. Phys.* B **14** 3584
[66] Fiebig M, Miyano K, Tomioka Y and Tokura Y 2000 *Appl. Phys.* B **71** 211
[67] Ogasawara T, Kimura T, Ishikawa T, Kuwata-Gonokami M and Tokura Y 2001 *Phys. Rev.* B **63** 3105
[68] Quijada M, Cerne J, Simpson J R, Drew H D, Ahn K-H, Millis A J, Shreekala R, Ramesh R, Rajeswari M and Venkatesan T 1998 *Phys. Rev.* B **58** 16093
[69] Jung J H, Kim K H, Noh T W, Choi E J and Yu J 1998 *Phys. Rev.* B **57** (R)11043
[70] Kim K H, Jung J H and Noh T W 1998 *Phys. Rev. Lett.* **81** 1517
[71] Okimoto Y, Katsufuji T, Ishikawa T, Arima T and Tokura Y 1997 *Phys. Rev.* B **55** 4206
[72] Kim M W, Jung J H, Kim K H, Lee H J, Yu J, Noh T W and Moritomo Y 2002 *Phys. Rev. Lett.* **89** 016403
[73] Kwon C, Jia Q X, Fan Y, Hundley M F, Reagor D W, Coulter J Y and Peterson D E 1998 *Appl. Phys. Lett.* **72** 486
[74] Hundley M F, Hawley M, Heffner R H, Jia Q X, Neumeier J J, Tesmer J, Thompson J D and Wu X D 1995 *Appl. Phys. Lett.* **67** 860
[75] Simpson J R, Drew H D, Smolyaninova V N, Greene R L, Robson M C, Biswas A and Rajeswari M 1999 *Phys. Rev.* B **60** R16263
[76] Kida N, Hangyo M and Tonouchi M 2000 *Phys. Rev.* B **62** R11965
[77] Ramirez A P, Schiffer P, Cheong S W, Bao C H, Palstra T T M, Gammel P L, Bishop D J and Zegarski B 1996 *Phys. Rev. Lett.* **76** 3188
[78] Khlopkin M N, Panova G K, Shikov A A, Sinyavskii V F and Shulyatev D A 2000 *Phys. Solid State* **42** 114
[79] Ren Y H, Zhao H B, Lupke G, Hu Y F and Li Q 2002 *J. Appl. Phys.* **91** 7514
[80] Kise T, Ogasawara T, Ashida M, Tomioka Y, Tokura Y and Kuwata-Gonokami M 2000 *Phys. Rev. Lett.* **85** 1986
[81] Ziese M 2001 *J. Phys.: Condens. Matter* **13** 2919
[82] Motome Y and Furkawa N 2001 *J. Phys. Soc. Japan* **70** 2802
[83] Liu X J, Moritomo Y, Nakamura A, Tanaka H and Kawai T 2002 *J. Phys. Soc. Japan* **71** 1648

[84] Orenstein J and Millis A J 2000 *Science* **288** 468
[85] Loeser A G, Shen Z X, Dessau D S, Marshall D S, Park C H, Fournier P and Kapitulnik A 1996 *Science* **273** 325
[86] Sun A G, Gajewski D A, Maple M B and Dynes R C 1994 *Phys. Rev. Lett.* **72** 2267
[87] Tranquada J M, Sternlieb B J, Axe J D, Nakamura Y and Uchida S 1995 *Nature* **375** 561
[88] Bonn D A, Liang R X, Riseman T M, Baar D J, Morgan D C, Zhang K, Dosanjh P, Duty T L, Macfarlane A, Morris G D, Brewer J H, Hardy W N, Kallin C and Berlinsky A J 1993 *Phys. Rev.* B **47** 11314
[89] Homes C C, Timusk T, Liang R, Bonn D A and Hardy W N 1993 *Phys. Rev. Lett.* **71** 1645
[90] Molegraaf H J A, Presura C, van der Marel D, Kes P H and Li M 2002 *Science* **295** 2239
[91] Carbotte J, Schachinger E and Basov D N 1999 *Nature* **401** 354
[92] Tinkham M 1996 *Introduction to Superconductivity* 2nd edn (New York: McGraw-Hill) ch 11
[93] Gray K E (ed) 1981 *Nonequilibrium Superconductivity, Phonons, and Kaptiza Boundaries* (New York: Plenum)
[94] Rothwarf A and Cohen M 1963 *Phys. Rev.* **130** 1401
[95] Rothwarf A and Taylor B N 1967 *Phys. Rev. Lett.* **19** 27
[96] Schuller I and Gray K E 1976 *Phys. Rev. Lett.* **36** 429
[97] Carr G L, Lobo R P S M, LaVeigne J, Reitze D H and Tanner D B 2000 *Phys. Rev. Lett.* **85** 3001
[98] Han S G, Vardeny Z V, Wong K S, Symko O G and Koren G 1990 *Phys. Rev. Lett.* **65** 2708
[99] Chekalin S V, Farztdinov V M, Golovlyov V V, Letokhov V S, Lozovik Yu E, Matveets A and Stepanov A G 1991 *Phys. Rev. Lett.* **67** 3860
[100] Demsar J, Podobnik B, Kabanov V V, Wolf Th and Mihailovic D 1999 *Phys. Rev. Lett.* **82** 4918
[101] Kabanov V V, Demsar J, Podobnik B and Mihailovic D 1999 *Phys. Rev.* B **59** 1497
[102] Demsar J, Biljakovic K and Mihailovic D 1999 *Phys. Rev. Lett.* **83** 800
[103] Kaindl R A, Woerner M, Elsaesser T, Smith D C, Ryan J F, Farnan G A, McCurry M P and Walmsley D G 2000 *Science* **287** 470
[104] Segre G P, Gedik N, Orenstein J, Bonn D A, Liang R and Hardy W N 2002 *Phys. Rev. Lett.* **88** 137001
[105] Feenstra B J, Schutzmann J, van der Marel D, Perez Pinaya R and Decroux M 1997 *Phys. Rev. Lett.* **79** 4890
[106] Demsar J, Hudej R, Karpinski J, Kabanov V V and Mihailovic D 2001 *Phys. Rev.* B **63** 4519
[107] Corson J, Mallozzi R, Orenstein J, Eckstein J N and Bozovic I 1999 *Nature* **398** 221
[108] Thorsmølle V K, Averitt R D, Maley M P, Bulaevskii L N, Helm C and Taylor A J 2001 *Opt. Lett.* **26** 1292
[109] Thorsmølle V K, Averitt R D, Maley M P, Hundley M F, Koshelev A E, Bulaevskii L N and Taylor A J 2002 *Phys. Rev.* B **66** 012519
[110] Brorson S D, Buhleier R, Trofimov I E, White J O, Ludwig Ch, Balakirev F F, Habermeier H-U and Kuhl J 1996 *J. Opt. Soc. Am.* B **13** 1979
[111] Pimenov A, Pronin A V, Schey B, Stritzker B and Loidl A 1998 *Physica* B **244** 49
[112] Averitt R D, Thorsmølle V K, Jia Q X, Trugman S A and Taylor A J 2002 *Physica* B **312/313** 86
[113] Hosseini A, Harris R, Kamal S, Dosanjh P, Preston J, Liang R, Hardy W N and Bonn D A 1999 *Phys. Rev.* B **60** 1349
[114] Corson J, Orenstein J, Oh S, O'Donnell J and Eckstein J N 2000 *Phys. Rev. Lett.* **85** 2569
[115] Averitt R D, Rodriguez G, Lobad A I, Siders J L W, Trugman S A and Taylor A J 2001 *Phys. Rev.* B **63** 140502(R)
[116] Averitt R D, Jia Q X and Taylor A J unpublished
[117] Demsar J, Averitt R D, Kabanov V V, Tracy L A, Trugman S A, Sarrao J L and Taylor A J 2002 *Ultrafast Phenomena* vol 12 at press
[118] RosePetruck C, Jimenez R, Guo T, Cavalleri A, Siders C W, Raski F, Squier J A, Walker B C, Wilson K R and Barty C P J 1999 *Nature* **398** 310
[119] Cavalleri A, Toth C, Siders C W, Squier J A, Raski F, Forget P and Kieffer J C 2001 *Phys. Rev. Lett.* **87** 7401